TEL AVIV UNIVERSITY
Raymond and Beverly Sackler
Faculty of Exact Sciences

# Isobaric simulation of a super-cooled lattice fluid

Thesis submitted as part of the requirements for the degree "Master of Science" (M.Sc.) in Tel-Aviv University

School of Physics and Astronomy
Department of Condensed Matter Physics

by

**Menachem (Nachi) Stern**

This thesis was performed and written under the supervision of

**Prof. Eli Eisenberg**

December 2012

# Abstract

When cooled beyond their melting point, materials enter the super-cooled fluid regime. The long-time fate of the super-cooled fluid could be either a crystalline stable state or an amorphous state known as glass. The nature of the glass transition, occurring at the deeply super-cooled fluid regime, remains one of the open questions in condensed matter physics. It cannot be explored directly in experiment or simulation, since the system relaxation time is expected to diverge at the transition point.

In an attempt to study the characteristics of the deeply super-cooled fluid regime, we suggest studying a relatively simple lattice fluid, the $N_3$ extended exclusion zone model. This system, devoid of long range interactions, is known to jam in amorphous states at high densities. To facilitate this effort, the implemented simulation scheme is isothermal-isobaric (constant pressure). Such a scheme is chosen since constant volume approaches are known to be less stable in the super-cooled regime.

The implementation of constant pressure simulators of lattice fluids involves some difficulty, as the volume difference between two sampled configurations must not be too large. We implement the model in constant pressure settings using two distinct approaches, one following Pendzig et al, the other due to Nies and Cifra. The first approach is found to be inadequate for large systems, while the second fares somewhat better. Super-cooled liquid samples are obtained in a pressure range unavailable before. However, the most deeply super-cooled samples we obtained are still far apart from the expected ideal glass transition point.

The super-cooled fluid regime is explored where samples are available. No signs of impending glass transition are found in measures such as the dynamical correlation functions. The crystallization processes (nucleation and nucleus growth) which limit us from obtaining deeply super-cooled samples are also studied. Both homogeneous and heterogeneous processes play a significant role in the formation of solid clusters. The clusters are found to be ramified in nature, an observation that could lead to deviations from classical nucleation theory.

## Acknowledgements

First of all I would like to thank my supervisor, Prof. Eli Eisenberg, for being a mentor and a friend, for his encouragement, guidance, and patience. Few are the people who could grant so much confidence and trust in the making of such a state-of-the-art endeavor. This work would not have been possible without his support. I am extremely grateful to him.

I am grateful to Dr. Asher Baram for his help in performing many of the analytic calculations, and for his frequent support in helping me grasp the subject matter of supercooled phenomena and glass formers.

I would also like to thank Prof. Abraham Nitzan for his support in the understanding of the partial grid point approach, and to Dr. Ziv Rotman on his help in implementing tools for exploration of dynamical correlation functions.

I like to express my gratitude to my supervisors at SNRC, Dr. Tamir Reisin and Dr. Shlomi Pistinner, for support of my doing the following work, and completing the requirements for the M.Sc. Their flexibility and understanding were crucial for the success of this work.

Finally, I would like to thank my mother, Hava, for her never-ending support, and my life partner, Shahar, for her love, support and encouragement during my studies.

# Table of Contents

# List of Figures and Tables

## Figures

## Tables

# Introduction

A liquid sample, cooled at a finite rate below its melting point, may avoid crystallization and remain liquid for significant times. This well-known type of process creates a super-cooled liquid, a metastable state whose existence is typically limited by nucleation and growth of small solid grains[1]. In some cases, fast enough cooling may lead the system beyond the glass transition to a stable non-solid configuration that cannot crystallize on any time-scale [2]. The resulting sample is generally locked in a state characterized by very slow dynamics and long relaxation times. When the relaxation time surpasses some conventional limit, we say that the sample went through a dynamic glass transition[3-6]. Further cooling of the sample would not facilitate equilibration to the crystalline state. Although a lot of progress has been made in the description of the deeply super-cooled state and dynamic glass transition, much is still poorly understood. The transition itself is regarded by some as a pure convention, having nothing to do with physics, but with our inability of setting up very long experiments[5]. Keeping this view in mind, many questions arise about a possible termination of the super-cooled state. In particular, a paradox raised by Kauzmann[7]: based on extrapolation of the super-cooled fluid heat capacity, it seems that at low enough temperatures the entropy of the (metastable) super-cooled state becomes lower than that of the (stable) solid. If such a phenomenon can be measured, it would imply the breaking of the third law of thermodynamics, as the liquid entropy cannot be smaller than the vibrational entropy of the glass at the same enthalpy[8]. Possible resolutions to the paradox include the introduction of a phase transition of the super-cooled fluid to a new phase at low enough temperatures, possibly the ideal glass[9-11]. Kauzmann himself has suggested that the supercooling phase is terminated by nucleation processes becoming faster than the fluid relaxation times. The point at which this transition occurs is known as the kinetic spinodal[7,12-13].

A true ideal glass transition, whether it exists or not, is thought to occur at experimentally inaccessible times (tending to infinity, due to the exponentially growing relaxation times). However, signatures of such a transition may appear at less deeply super-cooled samples, allowing exploration by experiment or numerical simulation. Both approaches have their own merits: experimental evidence is the only true proof of any theory in the scientific method. Furthermore, experiments allow exploration of quite long time scales, on the order of minutes,

hours or days. Their down side are our measurement limitations, in particular our inability to directly locate and track unique particles and structures. On the other hand, numerical simulations grant us broad freedom in measuring any observable. Unfortunately, as it is always dependent on theoretical modeling, simulation may digress from reality at important points. Moreover, current computation technologies place severe limitations on accessible simulation timescales[5,14]. These computational limitations become more severe as the microstructure of the sample and the interactions become more complex. Much effort has been exerted on both approaches, but both are far from being exhausted. In this work we present an attempt to simulate a simple system thought to exhibit glass-like behavior, a crucial quality in the search for deeply super-cooled state characteristics.

The quest for a suitable model for computer simulation of glassy behavior is guided by two principles. First, the model must be sufficiently simple to allow an efficient computation, thus providing access to longer time scales characteristic of glasses. Second, it should exhibit "jamming"[15], often related to geometrical complexity, leading to a dynamical arrest where there is no relaxation between different microscopic states of the system. Jamming is desirable, as it is expected to impede solid nucleation and growth, contributing to the stability of the super-cooled metastable state. Thus, the model must be simple for computational efficiency, but "complex" enough to have the quality of jamming. Rigid body systems constitute good candidates for such models, as they lack long range two particle interactions that complicate the dynamics. Another important element that separates rigid body models from more realistic liquids is the phase control parameter. Supercooling is usually thought of as a process involving temperature variations, hence the name. The same effect may be obtained at constant temperature, with variation of the density or pressure of the system[16]. Rigid body models usually utilize these parameters to control the system state instead of the temperature. The family of continuous hard sphere models in varying dimensionality has been a popular subject of numerical simulations. The important limiting characteristics of these systems have been resolved analytically, and different numerical protocols exist for preparing hard sphere samples in high density amorphous states. The hard sphere model is not very effective at creating arrested configurations, as simulations indicate that crystallization and dynamic relaxation take place on similar timescales[17], suggesting that the entropic barriers limiting solid nucleation are not sufficiently

high. As a result, numerical study of anything resembling a super-cooled state is done using theoretical scaffolding, e.g. the replica method[17]. A more direct approach to thermodynamic sampling of the super-cooled state may be obtained by a different family of rigid body models.

Lattice gas methods (LGMs)[18], also known as cellular automata, are a group of models utilizing discrete boolean grids to represent particulate systems. A grid site in a LGM may either be occupied by a particle or left void. Initially these models, introduced by Von Neumann and Ulam[19], were helpful to avoid detailed descriptions of small scale physics and also round-off errors typical of molecular dynamic simulations of continuous hydrodynamic systems. LGMs are studied using either molecular dynamics or lattice Monte Carlo simulations, where statistical mechanics replaces particle dynamics as the system motive force. The boolean nature of LGMs makes them a natural choice for implementing discrete rigid body models, the most trivial of which is the non-interacting lattice gas (NILG). In this model there is actually no repulsive interaction, and no other interaction whatsoever except for the no-double-occupancy rule. This simple model can be solved analytically[20]. More complex models introduce finite sized exclusion zones surrounding the particles. These models are conveniently named by the order of excluded neighbors: a model where the nearest neighboring grid site is excluded is named $N_1$, the second nearest $N_2$, and so on. Letting the number of excluded neighbors grow to infinity, while reducing the grid cell size to zero as to retain a constant exclusion zone volume, we reach the limit of the continuous hard sphere model. Such finite range interaction models have attracted attention for a long time[23], as melting of a solid sample seems to be dominated by short range repulsive forces. Rigid body extended exclusion zone models have been extensively studied on several geometries and dimensionalities (e.g. triangular lattices[21-22], simple cubic[24] etc.). The most popular subjects are the 2D square lattice models, $N_1$ being the model explored the longest and in the most throughout manner[23]. It is known to have a continuous Ising-like phase transition between an ordered and disordered state. This phase transition occurs on various 2D and 3D lattices. The next model in terms of exclusion radius is $N_2$, with exclusion extending to second nearest neighboring cells, also a well-studied model[24]. As opposed to $N_1$, it exhibits an important dependence on dimensionality. 2D $N_2$ has a continuous phase transition from a disordered to columnar phase: it is ordered in one direction but disordered on the orthogonal direction. In 3D however, $N_2$ exhibits a weak first order phase transition[25]. From here on we

shall concentrate on 2D models, as they are more straightforward to implement, and as mentioned earlier, simplicity is one of our guides to a suitable simulated model. As we are looking for a model to simulate super-cooled liquids, we are pressed to keep searching for a model which exhibits a clear first order phase transition. The simplest such model in the family of extended rigid body potential LGMs is the $N_3$ model.

As hinted by its name, $N_3$ is characterized by exclusion zones spanning the first, second, and third nearest neighboring grid cells. Compared to lower order models discussed before, $N_3$ attracted less attention. It is the simplest model in the family exhibiting a first order transition on a 2D square lattice. The first to explore this model were Bellemans, Nigam and Orban[26-27]. Heilmann and Praestgaard have shown that the $N_3$ exclusion zone is equivalent on the square grid to cross shaped pentamers[28], and theoretically proved the existence of a phase transition. Nisbet and Farquhar[29-30] used transfer matrix methods to support the existence of a first order phase transition in the square lattice $N_3$, while Orban and Van Belle[31] based their similar findings on series expansions. Eisenberg and Baram[32-33] later refined the application of R-matrix methods to accurately resolve the phase transition conditions of the model, and utilized random sequential adsorption-diffusion (RSAD) protocols to measure the random closest packing density of the system. Their research also indicated that a metastable super-cooled phase might exist in the $N_3$ model. Lately, Rotman and Eisenberg[34-35], conclusively verified R-matrix predictions with grand canonical Monte Carlo simulations, provided evidence for super-cooled-like behavior of dynamical correlation functions, and reported a dynamic glass transition at the predicted density. Oliveira et al. [36] have shown in simulations that an infinitely fast cooling of the $N_3$ system results in an amorphous state with a finite density of vacancies, or void grid cells. This body of research, and especially the latest works carried out since the beginning of the 2000's, provides encouraging data on the possibility of directly measuring deeply super-cooled states in the $N_3$ model on a square lattice. This relatively simple model exhibits first order phase transition, similar to physical liquid-solid transitions. Furthermore, rapid "cooling", simulated through RSAD protocols results in a well-defined dynamic glass transitions, accompanied by growing dynamic correlations. Finally, the "geometrically complex" nature of the model, necessary to dynamically arresting microscopic elements, is expected to impede solid nucleation and growth, possibly allowing super-cooled metastable states to exist for long times.

To this date a direct thermodynamical measurement of a super-cooled state in the $N_3$ model has been carried out only in constant volume settings. In such settings the equilibrium configurations for densities above the melting transition is a phase separated state, in which the system breaks up into two distinct phases, liquid and solid. Tracking this phase separation throughout the simulation is not trivial, and thus it is hard to determine whether the system is truly out of equilibrium and in the meta-stable glassy state. Another disadvantage of the constant-volume simulation is that they do not allow for an easy access to the compressibility (related to density fluctuations). There are some predictions suggesting that the compressibility might show signs of the nearing glass transition, and thus it is desirable to have this quantity accessible.

Another motivation for considering isobaric simulations is the hypothesis that in constant volume simulations relaxation to the phase separated state might be slower due to the following reason: any solid grain that happens to nucleate automatically leaves behind a lower density region where liquid constituent particles can flow and expand their volume. In the super-cooled phase, relaxation times depends very strongly on the density, thus the lowered density could result in an accelerated relaxation. As solid grains, or clusters, have more room around them, they can grow until stopped by mismatching surfaces of other clusters. The regions between mismatching clusters will stay at low density, hosting a liquid phase. A possible way of circumventing this process is to simulate the system in constant pressure and varying density.

Though rather well established in continuous systems[37-39], constant pressure Monte Carlo simulations for lattice fluids are a relatively new endeavor, carried out mainly in the field of chemistry of chain molecules and polymers[20,40-42]. The typical plague of discrete constant pressure Monte Carlo is the statistical inaccessibility of configurations with “large” super-microscopic volume variations. The discrete nature of LGMs requires unique implementation methods to avoid sampling large volume variations in the system. In this work we shall construct a constant pressure LGM, the $N_3$ extended exclusion zone model on a square grid, using two different approaches[20,42], in the intention of analyzing the super-cooled state in this model, and finding clues shedding light on the elusive thermodynamic ideal glass transition.

# 1. Isobaric Simulation of the $N_3$ Model

The system used in our study is called the $N_3$ model. This simple model incorporates a lattice, where each particle creates an exclusion zone which spreads up to its third nearest neighbor. The interactions between the particles are of "rigid body" type, and no long range interactions exist in the system beyond the exclusion zone. We wish to explore a two-dimensional representation of this system, on a square grid. The lattice and exclusion zone are depicted in the following figure:

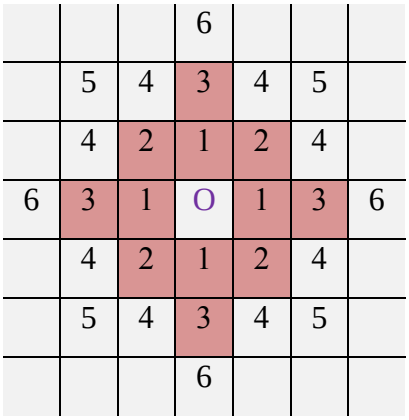


FIG 1 – The $N_3$ model. Particle location is indicated by "O". Digits indicate the enumeration of O's nearest neighbors. The darkened area represents the exclusion zone.

An alternative description of our particles is that of rigid cross-shaped pentamers[28], where even partial overlap of the particles is not allowed. This representation is shown in the following figure:

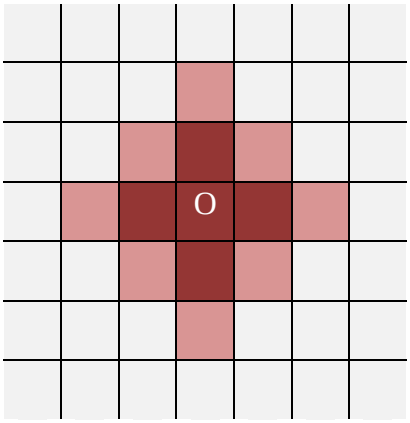


FIG 2 – The $N_3$ model cross-shape representation. Particle location is indicated by "O", and it occupies the area painted dark-red. Light red area represents the exclusion zone.

A defining feature of this model is the occurrence of amorphous jammed states. The geometric constraints of the particles allow them to be arranged in a periodic lattice structure, covering the entire given volume. These are the equilibrium configurations at high densities. However, high density $N_3$ systems may jam in amorphous states, leaving voids in between[36]. This feature lies in the core of the idea of utilizing the $N_3$ system as a simple model for glassy materials. Glasses may be metastable states relative to the crystal structure, but geometric and/or dynamical arrest mechanisms prevent them from decaying into the stable crystal state.

The two-dimensional $N_3$ system (on a square grid) has been surveyed in the past in analytical studies and numerical simulations. In low densities it behaves like an ideal gas with constant proportion of pressure to density. Higher density configurations see the pressure rises more rapidly, until a first order phase transition between a fluid and solid occurs at a density of $\rho_C \cong 0.158$[33], corresponding to a pressure of $P_c \cong 0.74$. The solid density just beyond the phase transition is also resolved to be $\rho_S \cong 0.191$. When cooled infinitely fast, using the Random Sequential Adsorption Diffusion (RSAD) procedure [32], the system jams in an amorphous glass-like state called the Random Closest Packing (RCP). In this state the density approaches a constant value of $\rho_{RCP} \cong 0.1716$. We are interested in understanding the behavior of the system within the super-cooled (metastable) regime, at pressures above the phase transition pressure. It is important to emphasize that the stable state of the system in these densities is not fluid, but a phase separated state with fluid and solid parts. These configurations (whether super-cooled or phase separated) have a higher density than $\rho_C$, but much lower than $\rho_S$. Using R-Matrix theory[34], a super-cooled fluid branch is shown to exist up to a termination density $\rho_T \cong 0.1717$, close to the random closest packing density. This density was therefore predicted to be the location of an ideal glass transition, or a kinetic spinodal[34]. The expected pressure for the ideal glass transition was estimated to be $P_T \sim 0.83$.

Previous numerical studies of the system used canonical or grand-canonical ensembles. As such, the volume of the system was constant in these studies. This work attempts to tackle the $N_3$ system from a different angle, by implementing an isothermal-isobaric (constant NPT) simulator of the system. The main advantage of such an approach is the possibility of detecting super-cooled states more easily. Furthermore the system may eventually leave a jammed state at long

times and crystallize, as opposed to the more subtle relaxation of the constant volume simulations into a phase separated state. Implementing an isothermal-isobaric simulator incorporates developing a technique to manage a system of variable volume, a nontrivial task when dealing with lattice fluids.

The main difficulty with variable volume Monte-Carlo simulations of lattice fluids is related to the need to sample states with different volumes. In general, the energy (Hamiltonian) of the system can be expressed as:

(1) $E = PV + f(T, N)$

In our model, $f(T, N)$ remains constant, and the difference between the energies of two configurations depend only on $PV$. The Metropolis criterion[43], defined in terms of the exponent of the difference between the energies of two configurations, then depends on the volume difference. In continuous systems, a sampled configuration may have a volume only slightly different than the reference configuration. This in turn allows the acceptance of new configurations with slightly higher volumes, enabling the system to effectively survey the phase space. Lattice fluid systems are however of a different breed, as the volume of such models is quantized. Therefore, the smallest variation is proportional to the surface area of the system, i.e. $\Delta V_{min} \sim V^{(d-1)/d}$, with $d$ the dimensionality (as seen in FIG 3). Although this minimal variation is sub-extensive, it grows with the system size. Once the energy difference associated with this minimal change is much greater than $k_B T$, the new configuration has a negligible probability to fulfill the Metropolis criterion, and is discarded, preventing an effective sampling of the phase space. The challenge in isobaric simulations of lattice fluid systems is to ensure that Metropolis steps will allow microscopic volume changes, associated with an $O(k_B T)$ energy difference, so that they are surmountable by the Metropolis criterion. In the following we present two methods developed to achieve this goal.

1.1. The partial grid point approach

As explained in the previous section, the main problem with Monte-Carlo sampling of volume variations is the large energy jumps between different volume configurations, due to the finite size of the grid points. Suppose our system consists of a 2D box, bounded by closed boundary conditions on all sides except the right boundary edge. This right edge can be moved inwards or outwards to facilitate system volume alterations. The volume alterations themselves are quantized by the demand that $L$, the length of the system, is integer. If we wish to expand our system, the smallest volume change would be the volume covered by the $D$ cells neighboring the right edge (see FIG 3).

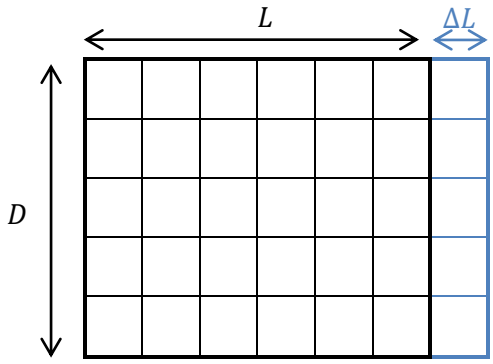


FIG 3 – A 2D lattice square system with sides (L, D). The smallest volume increment achievable by adding a full grid point to the right is $\Delta V = Dv_0$ ($v_0$ - the volume of one grid cell).

The volume increment in this scenario, although sub-extensive, clearly grows with the growth of the system. In the thermodynamic limit of infinite sized systems, the volume increment would diverge, disabling any Monte-Carlo sampling of configurations characterized by higher energy due to volume variation.

One approach to overcome this problem is the development of a protocol allowing the altering of the right edge boundary of the system by a step smaller than the length of one grid cell. Such an approach was developed by Pendzig, Dietrich & Nitzan[20] (here we present a modified version of this algorithm). The core of their approach is enabling the edge boundary to move in a "continuous" manner, instead of by quantized steps. To facilitate this type of movement, the occupation of a partial grid point near the mobile boundary must be defined. In essence, for every particle occupying a partial grid point, an energetic price must be paid. The specific energy form associated with each particle residing on a partial grid point may be chosen in different

ways. One simple and convenient choice is $E_S = -k_B T \cdot ln(k)$ (henceforth, $k_B T = 1$), where the partial occupation energy cost is linear in the temperature $T$, and $0 \leq k \leq 1$ is the fraction of the grid point inside the system boundaries. As we shall see later, this choice leads to a linear relation between the boundary position $\langle k \rangle$ and the density of particles occupying the partial grid points. When the extreme grid point is entirely outside of the boundary ($k = 0$), the price of occupying the grid point diverges and no particles reside there. On the other hand, occupying a fully included grid point ($k = 1$) costs no extra energy. The aforementioned structure is schematically depicted in FIG 4.

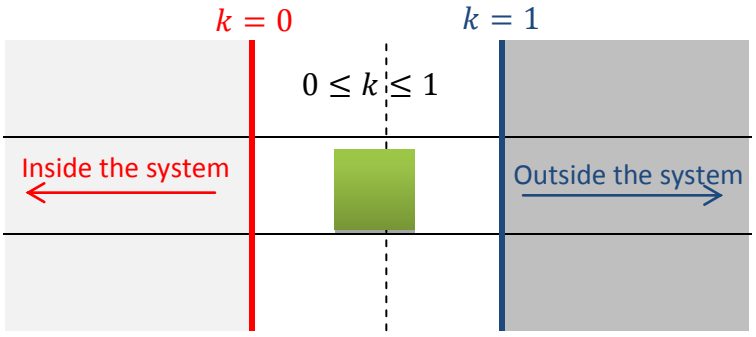


FIG 4 – Definition of a floating indicator $k$ at the systems mobile boundary. The particle, shown here as a green square, occupies a partial grid point with $0 \leq k \leq 1$.

The system consists of $N_3$ particles on a square lattice, as seen in the following figure. The linear dimensions are $L$ and $D$. The lattice unit cells are squares, whose volume is $v_0 = a_0^2$. In this work we always set $v_0 = 1$. The location of $N_3$ particle position is defined as the position of its central lattice point. The leftmost site is defined as $x = 1$, and the rightmost would be $x = L$. Cyclic boundary conditions are applied to the y-axis. On the x axis, however, where the mobile boundary on the right is present, we must impose closed boundary conditions. Note that a particle may be placed both at $x = 1$ and $x = L$ (each of these placements results in the left or right "wing" of the particle being outside of the system). In both cases we count such particles as $\frac{4}{5}'s$ of a particle. To enforce a constant pressure $P$, we introduce a piston that is located on the right, applying a constant force on the $x = L$ mobile boundary. The total (constant) number of particles in our system is $N$, and the total volume of the system is $V$. In the following discussions we will retain as much of these definitions as possible, with the exception of nomenclature changes related to the shape of the mobile boundary.

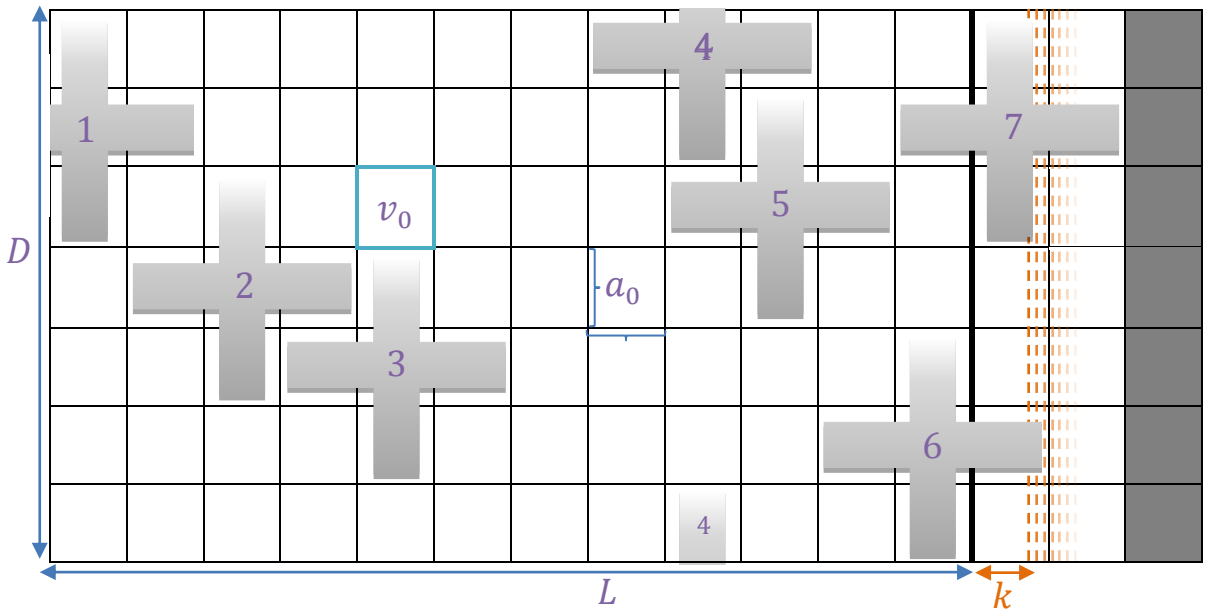


FIG 5 – Example of an isothermal-isobaric $N_3$ system.

The right boundary may move inwards or outwards, and change the total volume. Here $L$ signifies the position of the rightmost particle, and $k$ is a continuous variable that effectively expands the system by enhancing the length of the box. Conforming to the aforementioned definitions, $k$ may be larger than unity, representing that the mobile boundary is in fact not occupied at all. We shall thus define a complementary variable $k'$:

$$k' \equiv \begin{cases} k & k \leq 1 \\ 1 & k > 1 \end{cases}$$

The energy cost of partial grid point occupation, per particle, is therefore $E_S = -k_B T \cdot ln(k')$.

We now turn to determining the system energy, or Hamiltonian, for a general choice of $E_S$. First we stress that the particles interact only via hard core potentials. The hard core potential is implemented dynamically, by defining forbidden particle movements, and does not appear explicitly in the Hamiltonian. The only bulk contribution to the energy arises from the finite pressure exerted on the system from the right, $E = PV$. In addition, we add the abovementioned boundary occupation energetic cost. For now let us study a general specific occupation cost $E_S$. The full Hamiltonian is:

(2) $\quad E = PV + nE_S(k')$ ,

where $n$ is the number of particles occupying $x = L$ sites. We define a dimensionless energy scale $\delta \equiv \beta P D V_0$, where $\beta = (k_B T)^{-1} = 1$. In an approximately square box, $\delta \sim D \sim \sqrt{N}$. Now we may rewrite the Hamiltonian as follows:

(3) $$E(L,k,n) = PV_0 D(L+k) + nE_S = \frac{1}{\beta}\left(\delta L + \delta k + \beta n E_S(k')\right)$$

The probability of measuring the system in a state characterized by energy $E$ is proportional to the Boltzmann factor:

(4) $$P(E) \propto e^{-\beta E} = e^{-\delta L} \cdot e^{-\delta k} \cdot e^{-\beta n E_S(k')}$$

In the system defined above there are two types of degrees of freedom, particle locations and mobile boundary location. Both may change dynamically, as follows:

1) A particle may move one step at a time, to one of its four neighbors (up, down, left, right). The particle movement is allowed only if the new location is not excluded by neighboring particles.
2) The location of the mobile boundary may vary, expanding ($\Delta k > 0$) or contracting ($\Delta k < 0$) the system.

To fully define the simulation dynamical protocol, we need to fix the ratio between the rates of particles' movement and boundary movement. Pendzig et al. leave this rate unspecified, enabling the simulation to alter volume variations and particle movements in a predefined manner. Here, we choose to take the mobile boundary to be infinitely faster than the particles, so that the boundary instantly thermalizes with respect to the particles in its vicinity. This choice simplifies the treatment, as it allows us to integrate out the boundary variable $k$ analytically.

First we find the equilibrium distribution of the boundary location $k$ for a given particle configuration (and therefore a fixed value of $L$). The only dependence of the conditional probability distribution for $k$ on the particle configuration is through the occupation number $n$:

(5) $$P(k|n) \propto P\left(E(k,n)\right) \propto e^{-\delta k} e^{-\beta n E_S(k')}$$

The normalized (conditional) probability distribution function is therefore:

(6a) $$g_n(k) \equiv Q_n^{-1} e^{-\delta k} e^{-\beta n E_S(k')}$$

(6b) $$Q_n \equiv \int_0^\infty e^{-\delta k} e^{-\beta n E_S(k\prime)} dk = \int_0^1 e^{-\delta k} e^{-\beta n E_S(k)} dk + \int_1^\infty e^{-\delta k} dk$$

We now explicitly show how the particles' dynamics is fully characterized by the integrated quantities $Q_n$. Let us consider the movement probabilities of the particles in the system. The Metropolis probability is defined as:

(7) $$P_M(\Delta E) = \begin{cases} 1 & \Delta E \leq 0 \\ e^{-\beta \Delta E} & \Delta E > 0 \end{cases}$$

Different types of particle movements result in different energy changes $\Delta E$, and consequently different probabilities. Limiting ourselves to configurations which may be sampled by moving one particle at a time, there are 5 archetypes of new configurations (summarized in the following table). It is important to note that the mobile boundary position $k$ does not change while a particle movement takes place, thus the energy difference is only due to changes in $L, n$.

Table 1 – New sampled configuration archetypes.

| Archetype | Energy variation | Description |
|---|---|---|
| 1 | $\Delta n = 0$ , $\Delta L = 0$<br>$\Delta E_1 = 0$ | A particle moves in the bulk, away from the mobile boundary, or a particle moving near the boundary, parallel to it. |
| 2 | $\Delta n = -1$ , $\Delta L = 0$<br>$\Delta E_2 = -E_S(k') < 0$ | A particle moves from the boundary inwards, when other particles are still occupying the boundary. |
| 3 | $\Delta n = +1$ , $\Delta L = 0$<br>$\Delta E_3 = E_S(k') > 0$ | A particle moves into a boundary point from the bulk, when other particles are already occupying the boundary. |
| 4 | $\Delta n = 1 - n$ , $\Delta L = +1$<br>$\Delta E_4 = \frac{\delta}{\beta} - (n-1)E_S(k') > 0$ | A particle stretching the mobile boundary outwards by one grid point. |
| 5 | $\Delta n = n - 1$ , $\Delta L = -1$<br>$\Delta E_5 = -\frac{\delta}{\beta} + (n-1)E_S(k') < 0$ | The last boundary particle moves inwards, contracting the system by one grid point. |

According to the Metropolis criterion (7), particle moves of archetypes 1, 2 and 5, which are associated with a non-positive energy change, have unity probability of acceptance. The only two archetypes of movement that increase the system energy are 3 and 4. We may explicitly write the acceptance probability of moves of every archetype, and find their average.

A general function $f(k)$ can be averaged by:

(8) $\langle f \rangle = \int_0^\infty g_n(k) f(k) dk.$

Accordingly, the particle movements probabilities, averaged over boundary locations, are given by

(9a) $P_{1,2,5} = 1$

(9b) $\langle P_{1,2,5} \rangle = \int_0^\infty g_n(k) \cdot 1 dk = 1$

(10a) $P_3 = \exp(-\beta \Delta E_3) = e^{-\beta E_S(k\prime)}$

(10b) $\langle P_3 \rangle = \int_0^\infty g_n(k) \cdot P_3 dk = Q_n^{-1} \int_0^\infty e^{-\delta k} e^{-\beta(n+1)E_S(k\prime)} dk = \frac{Q_{n+1}}{Q_n}$

(11a) $P_4 = \exp(-\beta \Delta E_4) = e^{-\delta} e^{\beta(n-1)E_S(k\prime)}$

(11b) $\langle P_4 \rangle = \int_0^\infty g_n(k) \cdot P_4 dk = Q_n^{-1} e^{-\delta} \int_0^\infty e^{-\delta k} e^{-\beta E_S(k\prime)} dk = \frac{Q_1}{Q_n} e^{-\delta}$

Let us explore these probabilities more rigorously for our specific choice $E_S = -k_B T \cdot ln(k')$ :

(12) $Q_n(\delta) = \int_0^1 e^{-\delta k} k^n dk + \int_1^\infty e^{-\delta k} dk = \delta^{-(n+1)} \gamma(n+1, \delta) + \frac{e^{-\delta}}{\delta}$

Where $\gamma(a, z)$ is the incomplete Gamma function defined as:

(13) $\gamma(a, z) = \int_0^z e^{-x} x^{a-1} dx$

We are interested in the limit of large systems, where the dimensionless $\delta$ is large, thus it is useful to calculate the $\delta \to \infty$ ($n$ fixed, but >>1) limit of equation (12):

(14a) $\gamma(a+1 \ll z, z \to \infty) \cong a! \cong \left(\frac{a}{e}\right)^a \sqrt{2\pi a}$

(14b) $Q_n(\delta \to \infty) \cong \frac{n!}{\delta^{n+1}} + \frac{e^{-\delta}}{\delta} \cong \frac{\sqrt{2\pi n}}{\delta^{n+1}} \left(\frac{n}{e}\right)^n + \frac{e^{-\delta}}{\delta} \cong \frac{\sqrt{2\pi n}}{\delta^{n+1}} \left(\frac{n}{e}\right)^n,$

where the term $e^{-\delta}\delta^{-1}$ is negligible compared with $n!\,\delta^{-n-1}$, and Stirling's approximation was used to expand $n!$.

However, n and $\delta$ are dynamically related. The maximal occupancy is clearly bounded by the system width $D$ which scales with $\delta$. The boundary occupation is expected to be lower than the bulk density, due to the extra energy cost. Thus, the relation, in equilibrium, between the energy scale $\delta$ and the average boundary occupancy $\langle n\rangle$ is given by:

(15) $$\begin{cases} \delta = \beta P D v_0 = PD \\ \langle n\rangle \le \rho D \end{cases} \quad \rightarrow \quad \langle n\rangle \le \rho\delta/P$$

For an ideal gas (or extremely dilute $N_3$ system), $\beta P = \rho$. In finite densities, the pressure is always larger than the density, and therefore $\delta > \langle n\rangle$. In the thermodynamic limit it is expected that the occupancy fluctuates around $\langle n\rangle$, and large deviations will be rare. For simplicity of the following treatment, we define the ratio $\alpha \equiv \delta n^{-1}$ and expect it to be typically greater than unity.

Note that since $\langle n\rangle \sim \delta$, the proper limit to consider is not that of fixed $n$ and large $\delta$. Rather, both quantities diverge for large systems, with a fixed ratio $\alpha$. In this limit,

(16) $$Q_n\left(\delta \to \infty, \frac{n}{\delta}\ fixed\ and < 1\right) \cong \frac{n!}{\delta^{n+1}}$$

In addition, we calculate the average boundary position $\langle k\rangle$:

(17) $$\langle k\rangle_n = \int_0^\infty g_n(k)\, f(k) dk = Q_n^{-1} \int_0^\infty e^{-\delta k} (k')^n \cdot k dk =$$
$$= Q_n^{-1}\left[\int_0^1 e^{-\delta k} k^{n+1} dk + \int_1^\infty e^{-\delta k} k dk\right] \cong Q_n^{-1} \int_0^\infty e^{-\delta k} (k')^{n+1} dk =$$
$$= \frac{Q_{n+1}}{Q_n} \cong \frac{n+1}{\delta}$$

In the large system limit $1 \ll n \ll \delta$, $\langle k\rangle_n \cong n\delta^{-1} = \alpha^{-1} < 1$.
Thus we find that for large systems the mobile boundary is unlikely to be found in the region $k > 1$.

Next we consider the movement probabilities of the particles in the system. As described above, the only types of movements that are affected by the boundary energetic cost are $P_3$ and $P_4$.

(18a) $P_3 = \exp(-\beta \Delta E_3) = k'$

(18b) $\langle P_3 \rangle = \frac{Q_{n+1}}{Q_n} = \langle k \rangle_n$

The probability for acceptance of moves of type 3 is equal to the average boundary position in the thermodynamic limit. Crucially, $\langle P_3 \rangle$ scales as $\delta^{-1} \sim N^{-0.5} \to 0$ in the thermodynamic limit, but the number of possible $P_3$ moves scales as $N^{0.5}$, leading to scalable relaxation times.

(19a) $P_4 = \exp(-\beta \Delta E_4) = e^{-\delta}(k')^{1-n}$

(19b) $\langle P_4 \rangle = \frac{Q_1}{Q_n} e^{-\delta} = \frac{\delta^{n-1}}{n!} e^{-\delta}$

To evaluate $\langle P_4 \rangle$ in the large system limit, we use Stirling's approximation and find:

(19c) $\langle P_4 \rangle = \frac{\delta^{n-1}}{\sqrt{2\pi n}\left(\frac{n}{e}\right)^n} e^{-\delta} = \sqrt{\frac{1}{2\pi}} \left(\frac{\delta}{n}\right)^{n-1} n^{-1.5} e^{n-\delta} = \sqrt{\frac{\alpha}{2\pi}} \frac{\alpha^{\delta \alpha^{-1}} e^{-\delta(1-\alpha^{-1})}}{\delta^{1.5}} =$

$$= \sqrt{\frac{\alpha}{2\pi}} \delta^{-1.5} e^{-\delta\left[1-\alpha^{-1}(1+\ln(\alpha))\right]}$$

For $\alpha > 1$, $c(\alpha) \equiv 1 - \alpha^{-1}(1 + \ln(\alpha))$ is positive and $\langle P_4 \rangle$ decays at least as fast as $e^{-\delta c(\alpha)} \delta^{-1.5} \sim N^{-0.75} e^{-\sqrt{N} c(\alpha)}$ in the large systems limit.

The previous observation casts an unavoidable doubt on the applicability of the partial grid point approach. The exponential system size dependence may prevents us from correctly describing the $N_3$ system in the thermodynamic limit where $N \to \infty$.

The physical meaning of the failure depicted in (19) is that even when the boundary is fully occupied with bulk density, the averaged location of the mobile boundary is $\langle k \rangle_{\langle n \rangle} < 1$. Thus, for large systems, the probability of having a configuration with $k > 1$, necessary to expand the boundary is exponentially small. As $\delta$ linearly depends on the pressure $P$, it is expected that relaxation times will also grow exponentially fast with it.

We therefore conclude that the partial grid point approach cannot be scaled up to large systems. Although the approach was developed to treat constant pressure lattice fluids, it proves incapable of simulating such models in the large system limit.

It should be noted that although our implementation used an infinitely fast boundary, setting a higher boundary relaxation time, along the lines of Pendzig et al.[20], would not solve the problem. In such settings, when the mobile boundary is fully occupied, it will fluctuate around its average location $\langle k \rangle_{\langle n \rangle}$ most of the time. The grid cell itself would require finer quantization the larger the system, as to be energetically capable of sampling higher volume configurations. This in turn would make spontaneous boundary jump exponentially rarer, impossible in the thermodynamic limit. In conclusion, implementing the "full" partial grid point approach by separating the particle and boundary movement would not solve the inapplicability of the method in the thermodynamic limit. The method may be used for small systems (for which some results have in fact been obtained), but larger systems cannot be explored due to the rapidly rising relaxation times. Relying on the aforementioned considerations, the partial grid point approach has only limited use, and a radically different approach is in order.

In principle, it may be possible to modify the partial grid point approach using a different choice of $E_S$, one that will allow all transition probabilities to scale up reasonably with system size. Such a modification must be chosen carefully. Consider the function $R(k) \equiv exp\left(-\beta E_s(k')\right)$. From physical considerations it must be a monotonic function of $k$. It seems reasonable to have it approach zero for $k \to 0$, and unity for $k \to 1$. It can be shown that strongly convex selections of $R(k)$ near $k = 1$ reduce the decay rate of $\langle P \rangle_4$ due to increased system size. Unfortunately, convexity anywhere between zero and unity results in lowering $\langle P \rangle_3$.

## 1.2. The elastic boundary approach

The first approach we reviewed used an energy cost protocol to view the boundary discretely sized grid cell as a "continuous" point indicator. This should have allowed sampling volume variations that do not scale up with system's size, resulting in transition probability that does not vanish in the thermodynamic limit. However, as implemented, the partial grid point approach did not live up to the expectations. A second method to achieve this goal is to let the mobile

boundary accept an arbitrary shape, not necessarily a straight line. For example, suppose the system shape at the current configuration is rectangular. We now sample a new configuration where the mobile boundary shifts by one grid cell, but only at one point (See FIG 6).

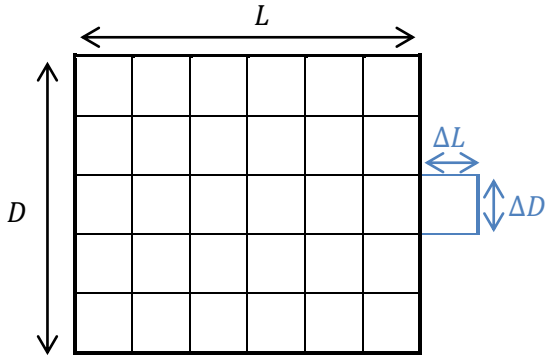


FIG 6 – A 2D lattice system with sides (L, D). The smallest volume increment achievable by adding a single grid point to the right is $\Delta V = 1$. This however requires the mobile boundary to bend and change its form.

The curved mobile boundary may be harder to implement than its straight counterpart, but the advantage of this approach in the thermodynamic limit is clear. It was first utilized by Nies & Cifra[42] to implement constant pressure Monte Carlo simulations in polymers. Using this method, a particle must always occupy a whole grid point, and there is no need to employ a correction of the form used by the former quasi-continuous approach. To implement such a boundary we must change our notation for its location. Up until now the mobile boundary was located at a single x-axis point, justifying the constant indicator $L$. In this approach we use a generalized indicator $L(y)$ to locate the mobile boundary position anywhere on the parallel axis. We still note that the grid point dimensions are quantized, such that $L(y)$ is integer for every $y$. It must be noted that a boundary occupying particle may move up or down, possibly expanding the system by $\Delta V > 1$ (see in the following FIG 7).

The Hamiltonian of this system simplifies to its trivial form $E = PV$. A possible disadvantage of this method is the finite probability of sampling configurations with wildly curved boundaries. These configurations may "trap" the system, by entropically favoring large volume variations over the minimal volume variations allowed by this method. An example of a "trapped" system is shown in FIG 7.

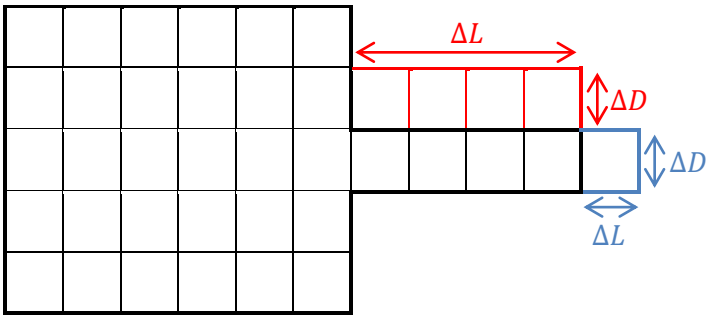


FIG 7 – A 2D lattice system with highly curved mobile boundary. Two possible variations in the bulge may change the volume by 1 (blue), but six may change the volume by 2-4 (red).

A natural approach to mitigate the trapping of the system in such configurations is to augment the Hamiltonian with a surface tension term.

(20) $E = PV + \sigma A \qquad \{\sigma \geq 0\},$

Where $\sigma$ is the non-negative energy scale of the surface tension, and $A$ the area of the system boundary. In our 2D system, the area degenerates to the length of the mobile boundary. Aiming at enforcing an almost straight boundary, we choose the surface energy term to be proportional to the local squared curvature at a point :

(21) $\mathcal{A}(y) \equiv [L(y+1) - L(y)]^2$

The total surface area is the sum of all these local curvatures. The Hamiltonian then takes the form:

(22) $E[L(y)] = PDv_0 \sum_y L(y) + \sigma \sum_y [L(y+1) - L(y)]^2$

This form adds an intensive energy cost to volume changes that increase the local curvature. Such a term may inhibit volume variations, but not in a way that scales up with the system size. Careful selection of the surface tension energy scale $\sigma$ is in order. A practical guideline for setting $\sigma$ may be described as follows: its value should be low enough to allow local curvature, but high enough to exclude "macroscopic" topography in the system.

The first condition may easily be implemented. Consider again the configuration variation depicted in FIG 6. The new configuration expands the system by one grid cell, and increases the local curvature on both its sides. The total energy variation is:

(23) $\Delta E = PDv_0 + 2 \cdot \sigma$

Requiring that the surface tension does not impede this microscopic variation, we set the condition $\sigma < 0.5PDv_0$. In the $N_3$ system the particles are somewhat more elaborately formed, and the typical smallest volume variation requires expansion of 3 whole grid cells. Thus the relevant surface tension condition becomes $\sigma < 1.5PDv_0$. The low limit condition on $\sigma$ is harder to define explicitly. We may however use trial and error to set its value as to avoid global "macroscopic" topography which could entropically trap the system (FIG 7). A simple way to find a suitable scale is to evaluate the average local curvature of the system:

(24) $\bar{a}(\sigma) = \frac{1}{D}\sum_y |L(y+1) - L(y)|$

Note that this function is different than (21). It uses absolute value differences instead of squared differences. As this is a purely diagnostic tool, it takes no role in the dynamics, but its interpretation is somewhat easier. If this average curvature is lower than unity, the particles are neatly ordered in a straight line, since the surface tension is too high to have significant curving anywhere. This limit is undesirable, as it brings us back to the straight boundary, resulting in the same difficulty seen within the partial grid point approach. On the other hand, if the local curvature is much larger than unity, the boundary is macroscopically curved. What we seek is a local average curvature slightly higher than unity. Values in the range of 1-1.2 were found to be appropriate using trial and error. These systems are found to have no macroscopic topographical features, but an average particle is not neatly ordered next to its neighbors.

We must still fully define the location of the mobile curved boundary $L(y)$. In principle, the boundary could be considered as an independent set of degrees of freedom, and the relative change rates of the two types of degrees of freedom (boundary and particles) is to be determined. We choose a simpler approach: the local mobile boundary is always attached to the furthest lying particle. For example, if the last $N_3$ particle (highest $x$ value) in some vertical position is placed in $(x, y)$, the local boundary position would be $L(y) = x + 1$. This choice allows us to consider only particle movements in the numerical scheme, as we had in the partial grid point approach.

# 2. Basic Results and Method Comparison

In this chapter we will detail the basic results obtained by our isothermal-isobaric simulation protocol concerning the $N_3$ system, and discuss the advantages and disadvantages of each implemented theoretical method.

As mentioned, the system is isothermal-isobaric, at constant temperature $T$, Pressure $P$, and particle number $N$. It is customary to denote these conditions as constant $NPT$. To approach the thermodynamic limit, we wish $N$ to be as large as computational resources allow. In addition, in order to minimize finite-size effects, it is favorable to have the system shape close to that of a square. The length of the system in our NPT ensemble is a dynamic quantity, but we set the width such that at the end of the density relaxation the system would be approximately square. A simple way to achieve this setting is to estimate in advance the equilibrium density of the system (for super-cooled system $\rho \sim 0.16 - 0.17$), and set the system width $D$ such that its square produces that density:

(25) $$D \cong \sqrt{\frac{N}{\rho}}$$

Since the only term in the system's energy is the pressure-volume term ($E = PV$), the system's Equation of State (EoS) depends on a single parameter $\rho$(P,T)=$\rho$(P/T). We therefore choose to set the temperature unit to one, and present the EoS as a function of pressure. The length units are set such that the lattice constant and the area of a single grid cell is unity.

## 2.1. The partial grid point approach

We first implemented the "partial grid point" approach, following Pendzig et al.[20] This approach utilizes a simple straight mobile boundary, but one which may advance continuously into the last lying grid cell. Particle occupation of the partial cells costs energy. We note again that in our implementation the boundary adapts (or thermalizes) infinitely fast compared with the movement of particles occupying partial grid cells. As a first validation of the simulator, we reproduce the known equation of state of the $N_3$ system in the fluid regime. At very low

pressures we expect to see an ideal gas behavior of the form $\rho \sim P$. As the pressure increases, the density should deviate from an ideal gas and become sub linear, until a first order phase transition occurs in $P \sim 0.74$. The calculated results are presented in the following figure, compared to $N_3$ EoS obtained from a constant-volume grand canonical simulation[33].

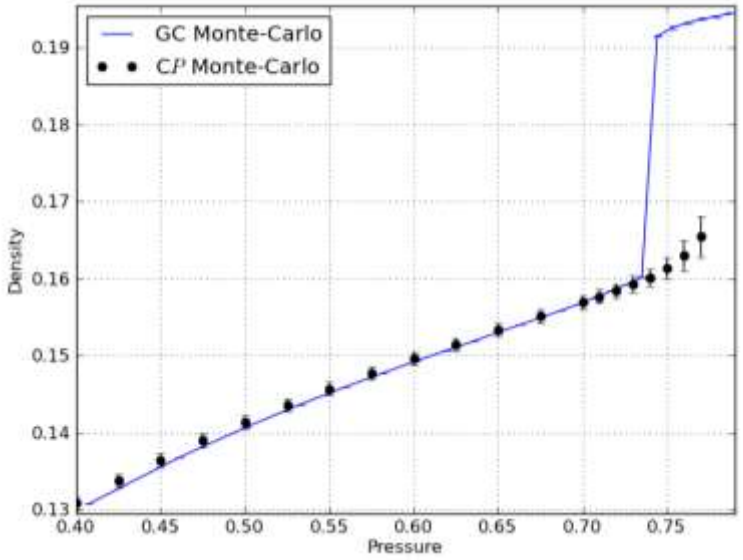


FIG 8 – $N_3$ equation of state (density vs. pressure), obtained by the partial grid point approach ($N = 500$).

We find that the simulator reproduces the $N_3$ equation of state below the phase transition pressure. We have simulated the system with initial low ($\rho \sim 0.12$) or high ($\rho \sim 0.17$) density settings, and concluded that the good agreement is obtained regardless of the initial condition of the system. However, problems with the partial grid point method arise when we increase the system size (number of particles) and approach the phase transition pressure. In the next figure we present relaxation times obtained in equilibration trial runs of systems at different pressures and sizes:

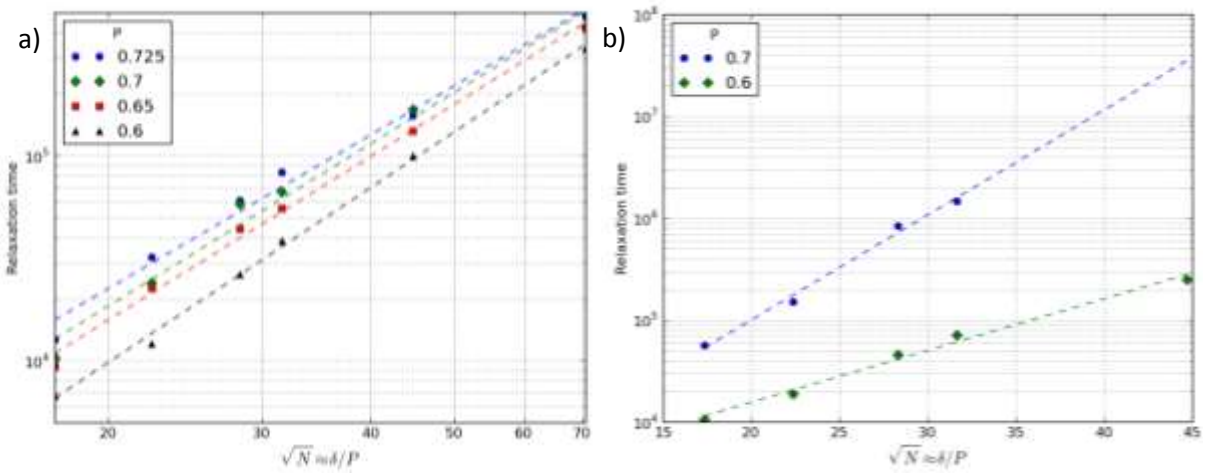


FIG 9 – Equilibration trials: Relaxation times of systems of different size and pressure. Each line represents a single pressure value. a) Fluid-like initial conditions ($\rho_0$~0.12); relaxation times rise as a power law with system size. b) Glass-like initial conditions ($\rho_0$~0.17); relaxation times rise exponentially with the energy scale $\delta$.

We find that equilibration times for a dilute initial condition increase dramatically with system size for pressures in proximity of the phase transition pressure. This rise can be approximated by a power law of the system size $\sim N^{2.5}$. The relaxation time also exhibits a mild dependence on pressure. Starting at a high density of $\rho_0$~0.17, the relaxation time dependence on system size is exponential. For $P = 0.6$ the relaxation time grows as $\sim exp\left(0.12\sqrt{N}\right)$, while for $P = 0.7$, it grows as $\sim exp\left(0.23\sqrt{N}\right)$. These exponents qualitatively agree with results obtained from (19). We thus confirm that this simulation approach is problematic for exploring the $N_3$ system in the thermodynamic limit.

Although generally inapplicable for the description of large systems, the partial grid point approach can be utilized to obtain results for medium sized systems. The following figure shows the Equation of State, as calculated for a system of $10^3$ particles. It is found that even for this system, which converges to the right EoS regardless of the initial condition in the fluid regime, the post transition regime may be poorly described. The simulation duration was not long enough for the density to converge to the same value from different initial conditions. Due to this problem, we are reluctant to trust these results, and are coerced to use a different approach for the more interesting post transition super-cooled regime. Relying on the aforementioned considerations, the partial grid point approach will no longer be of use in the rest of our work.

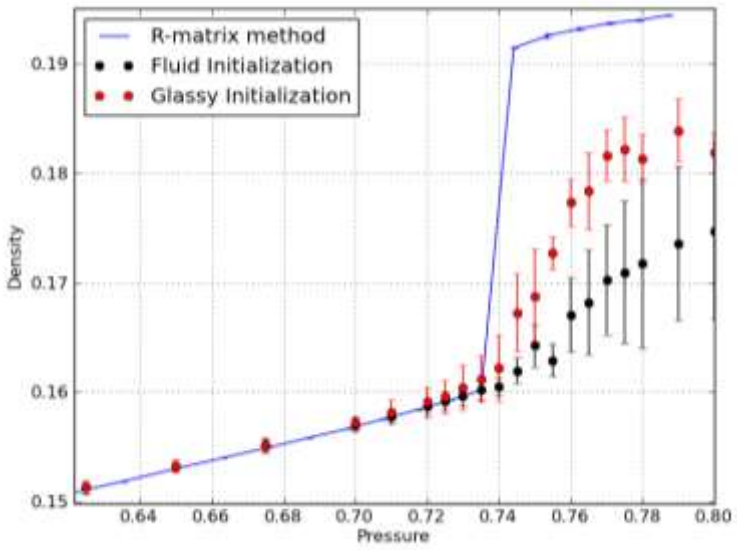


FIG 10 – Long time densities of systems initially setup with different initial conditions, for different pressures. Black dots: "Fluid system" initialization or low density; Red dots: "Glassy system" initialization, or a high density. Low pressure show no differences, but there is a growing density discrepancy in the high pressure regime, beyond the phase transition ($N = 10^3$).

## 2.2. The elastic boundary approach

As the partial grid point approach failed, we turned to the elastic boundary approach of Nies and Cifra[42]. Though it is considerably more difficult to implement, its Hamiltonian is simpler, and naturally temperature independent. The following figure presents the mid pressure equation of state obtained by using the elastic boundary approach with zero surface tension:

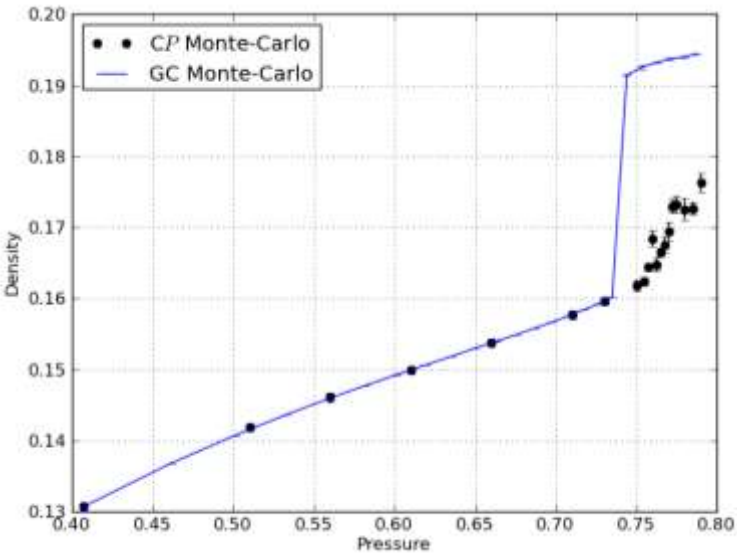


FIG 11 – $N_3$ equation of state, obtained by the elastic boundary approach ($N = 10^3$).

Again, the equation of state compares well with the grand canonical results[35] in the liquid phase. We can fortunately report that the elastic boundary approach is devoid of the equilibration problem that occurred in the partial grid point approach; the new simulation approach generally equilibrates to the same (liquid phase) density regardless of the initial condition and size of the system. The following figure illustrates the relaxation time dependence on the system size, for the relevant pressure values.

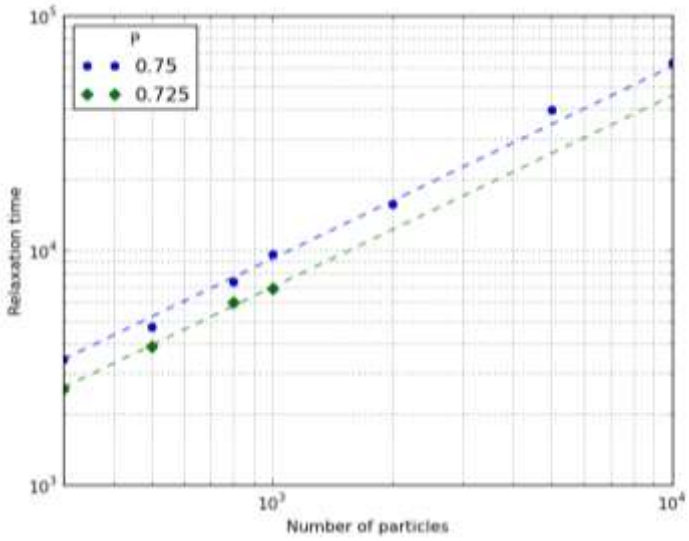


FIG 12 – Relaxation time for systems of different sizes and pressures. The initial condition used for the relaxation time measurements was $\rho_0 \sim 0.14$. Relaxation times rise sub-linearly with system size, as $\sim N^{0.8}$.

This observation is of course very encouraging, as it gives us hope of successfully simulating a lattice fluid system in the thermodynamic limit. We may now move on to discuss the high pressure behavior of our system in the super-cooled fluid regime, which is inaccessible to the grand canonical simulation.

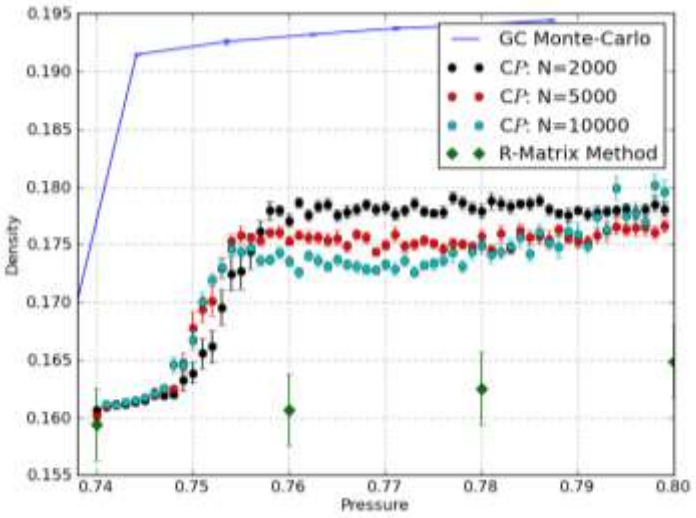


FIG 13 –Equation of State in the high pressure regime, for systems of different sizes.

The first obvious result is that the constant pressure system avoids the first order phase transition for very long times. Compared to the density relaxation times (FIG 12), the Equation of State remains stable for at least 3 more orders of magnitude in time. This meets our general expectations that the system would not be able to crystallize due to the dynamical arrest between ill ordered particles. Instead, the continuous liquid equation of state extends deeper into the high pressure regime. Once the pressure increased above ~0.75, the system experiences what seems to be a different 'phase transition', which appropriately narrows the larger the system becomes. At this stage the nature of the high pressure phase is not clear, but it does not seem to fit the super-cooled liquid description of the R-Matrix theory[34]. Most notably, the observed ‘phase transition’ occurs at a pressure much lower than that predicted by R-Matrix theory ($P_T \sim 0.83$).

To clarify the details of the state the system enters in the high pressure regime, we must present equilibrium system snapshots. In the next figure four such states are shown for pressures below and above the supposed phase transition at $P = 0.75$.

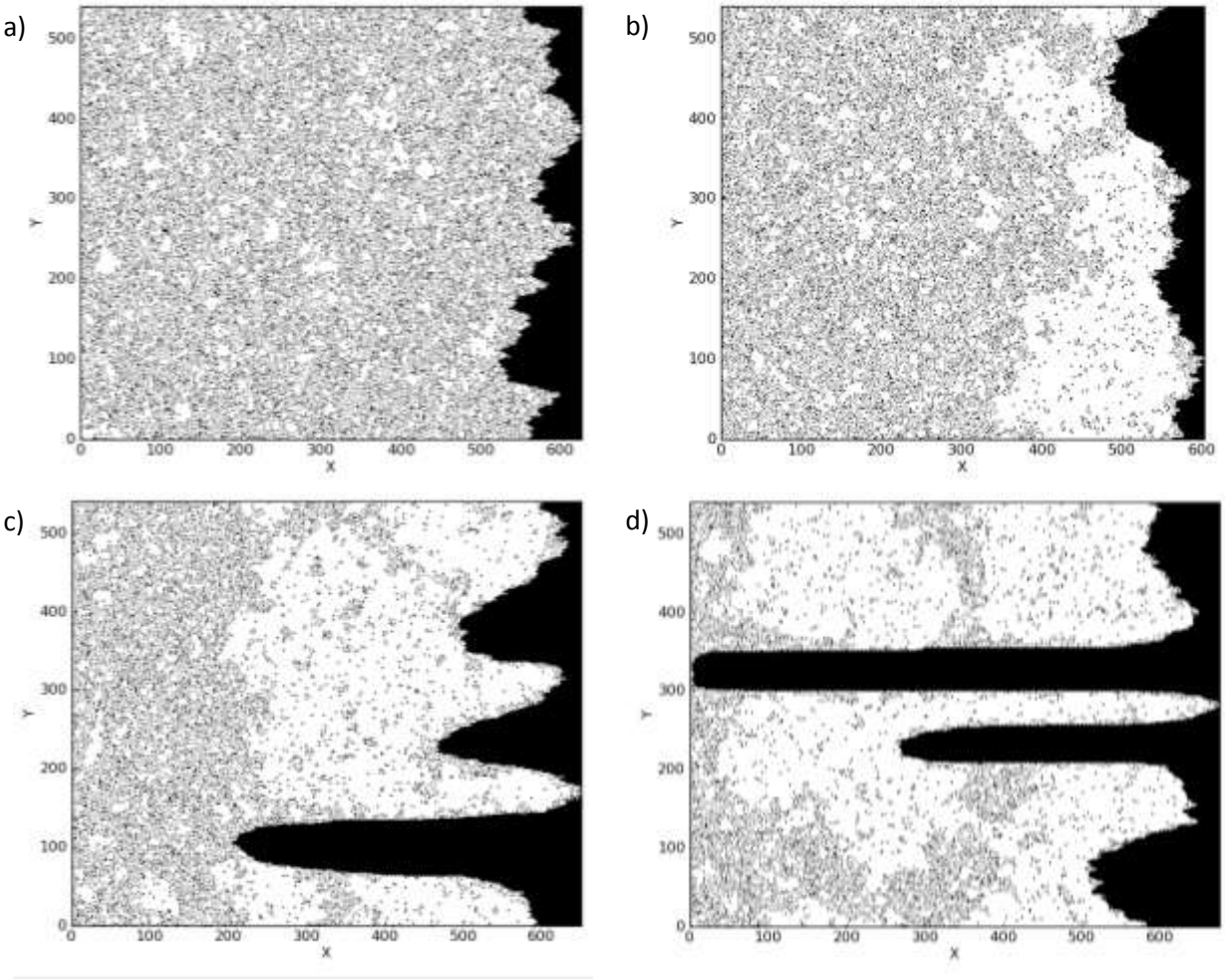


FIG 14 – Equilibrium snapshots of systems with $N = 5 \cdot 10^4$ ($\sigma = 0$). a) $P = 0.74$, b) $P = 0.755$, c) $P = 0.77$, d) $P = 0.8$. White dots represent particles, Black spots represent voids.

In FIG 14 we find various interesting phenomena. At pressures lower than about $0.75$, the system boundary exhibits a significant curvature. The boundary clearly does not resemble the straight line we had in the partial grid point approach. A detailed look into these configurations reveals that they indeed seem to be super-cooled liquids. As we shall see later, they contain no large scale particle clusters. By increasing the pressure over the transition at $0.75$, two distinct processes occur. The first is a gradual curving of the boundary, promoting macroscopic topographical features as hills and valleys. As explained in the first chapter, this phenomenon stems from entropic trapping of configurations. If a macroscopic feature occurs it has a low probability of being spontaneously dissolved (see FIG 7). The second process seems to dominate the occurrence of higher density: clusters start to aggregate near the mobile boundary

(recognized in FIG 14 (b) as bright white areas). The 'phase transition' implied by the density jump seems to originate in heterogeneous nucleation near the mobile boundary, resulting in phase separation between a dense equilibrium fluid and a solid. Further increase of the pressure, up to $P{\sim}0.76$ increases the relative abundance of clusters, thus increasing the average density. At even higher pressures, the system no longer becomes denser, but the boundary curvature increases in a seemingly unbounded fashion. This process continues until the system splits into non-interacting subdomains, separated by stable macroscopic voids.

To counter the macroscopic curvature we utilize the surface tension term in (20). The next figure displays the local average curvature (24) as a function of the surface tension scale $\sigma$.

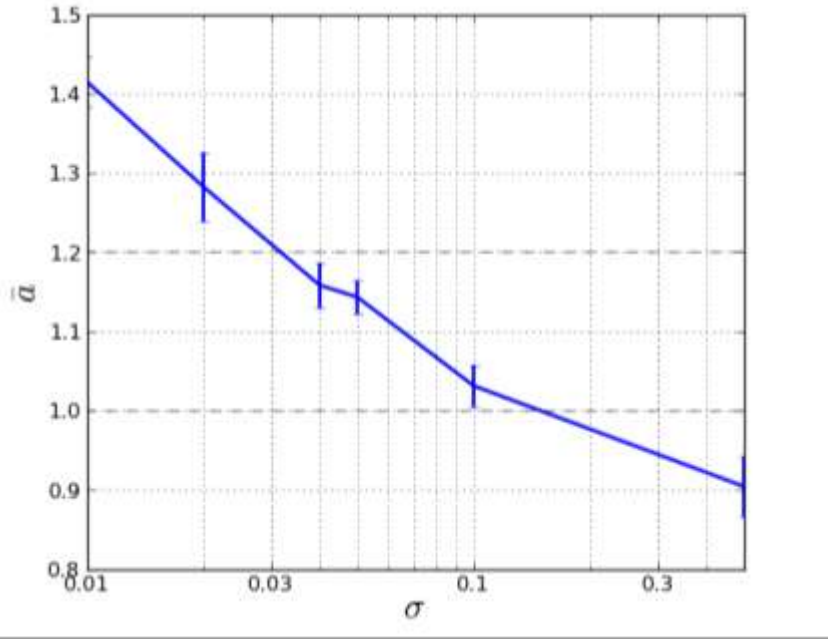


FIG 15 – Average local curvature $\bar{a}$, as a function of surface tension energy scale ($P = 0.75$). The desirable value of $\bar{a}$ is found to be in the range $1 - 1.2$ (shown with dashed lines).

In the previous chapter we argued that a suitable value $\sigma$, in terms of the boundary curvature, results in $1 \lesssim \bar{a} \lesssim 1.2$. From FIG 15 it is evident that an appropriate choice for the surface tension energy scale is $\sigma{\sim}5 \cdot 10^{-2} - 1 \cdot 10^{-1}$. We have explicitly checked that this parameter range is appropriate for the whole pressure/density range of interest. Although the surface tension scale range is, strictly speaking, pressure dependent, this dependence is very slow in the

region of interest of $P{\sim}0.75$. The following figure presents long-time system snapshots with this limiting surface tension scale.

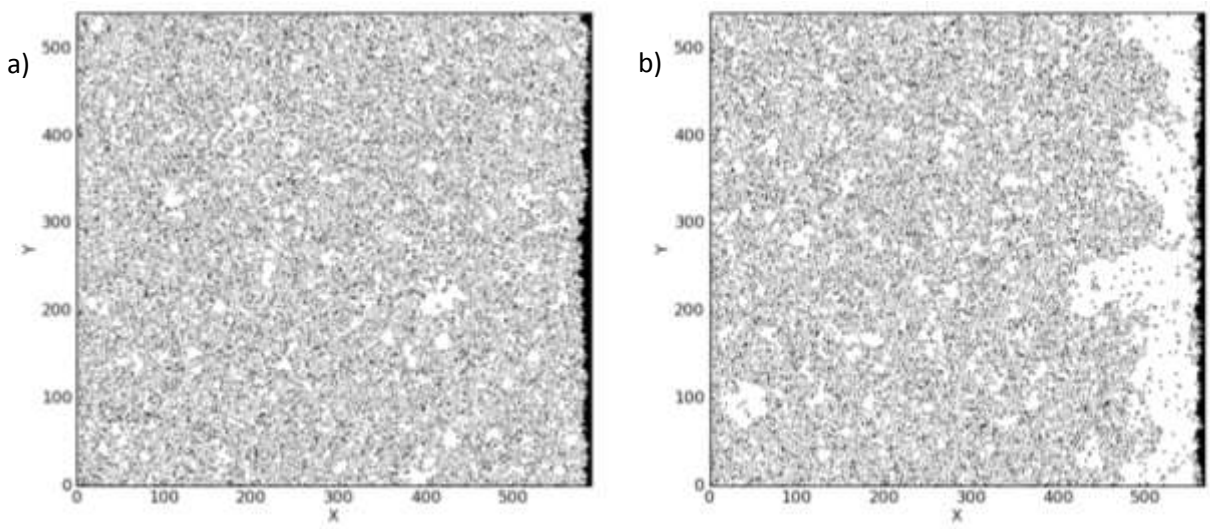


FIG 16 – Equilibrium snapshots of systems with $N = 5 \cdot 10^4$, $\sigma = 5 \cdot 10^{-2}$. a) $P = 0.74$, b) $P = 0.8$.

Implementing a surface tension term successfully restrains the curvature of the mobile boundary, and keeps it relatively straight at all times. It must be noted that as long as the surface energy scale is low enough, this method does not suffer from the difficulty encountered with the partial grid point approach. Boundary particles may easily move out and locally increase the system volume, but macroscopic curvature is disabled by the elastic character of the mobile boundary.

Although boundary curvature is effectively restrained by the surface tension, another problem arises – accelerated nucleation near the mobile boundary occurs at sufficiently high pressures (FIG 16(b)), resulting in a high density "wall" along the boundary. This heterogeneous nucleation is the process limiting the super-cooled metastable branch at high pressure. To better understand the formation of these heterogeneous features, we explore the system density and mobility as a function the horizontal location $x$. The density $\rho(x)$ is clearly defined, but there are many ways to quantify mobility, and here we choose a simple one. The system mobility is the number of allowed movements per particle. At the ideal gas limit each particle has exactly 4 allowed moves. In the other limit, the solidified sample (or ideal glass), all particles are locked in place and the mobility is zero. In the $N_3$ simulations it is expected that the mobility would

initially be rather high, and it should drop as the system density increases. Spatial variation in mobility might be correlated to nucleation and the rate of cluster formation. For example, the mobility near the mobile boundary is expected to be much higher than deeper inside the sample. This results from the fact that there are no particles blocking the way from the outside. The higher mobility near the boundary explains why heterogeneous nucleation is much more rapid than homogeneous nucleation, as particles near it may move at much higher rates and cluster together. Deeper in the sample, higher mobility is linked to lower density, which enables slow but significant homogeneous nucleation and cluster growth.

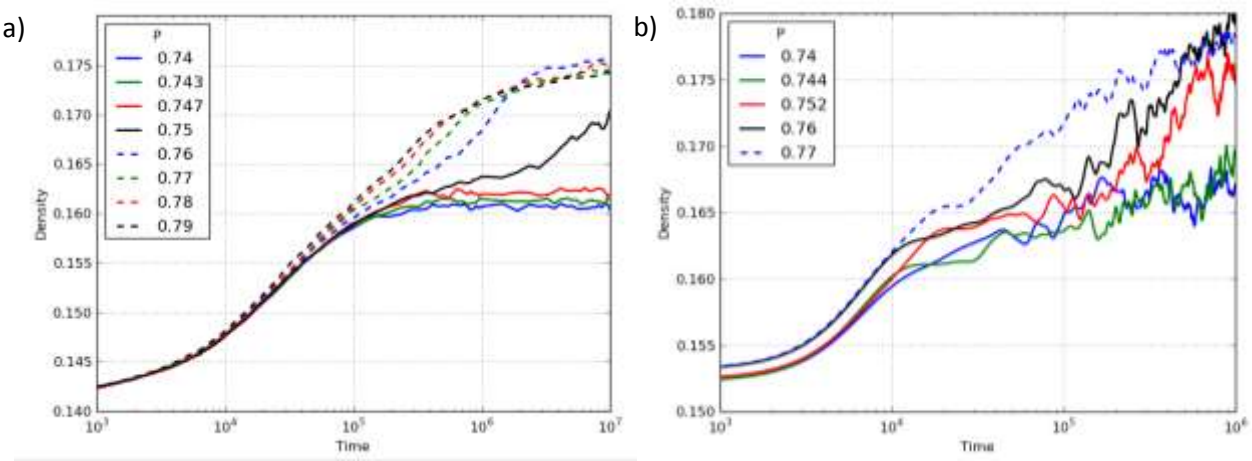


FIG 17 – Density vs. time graphs for systems at various pressures above the transition. a) $N = 5 \cdot 10^3$, $\sigma = 0$, b) $N = 5 \cdot 10^2$, $\sigma = 5 \cdot 10^{-2}$.

In order to study the interplay between relaxation towards the super-cooled phase and the nucleation processes along the mobile boundary, let us look at FIG 17. Below $P = 0.75$ we observe that systems relaxes to a dense state, with relaxation time $t \sim 10^5$. Then, these dense configurations seem stable for more than an order of magnitude in time. On the other hand, higher pressure configurations exhibit gradual density increase with no signs of relaxation. Moreover, the elastic boundary (with $\sigma \sim 5 \cdot 10^{-2}$), makes the system unstable even at a lower pressure of $0.748$.

In order to understand the processes underlying the system instability, we look at the following figure that presents density and mobility profiles across the "horizontal" coordinate $x$ (normal to the mobile boundary) for different times and pressure realizations.

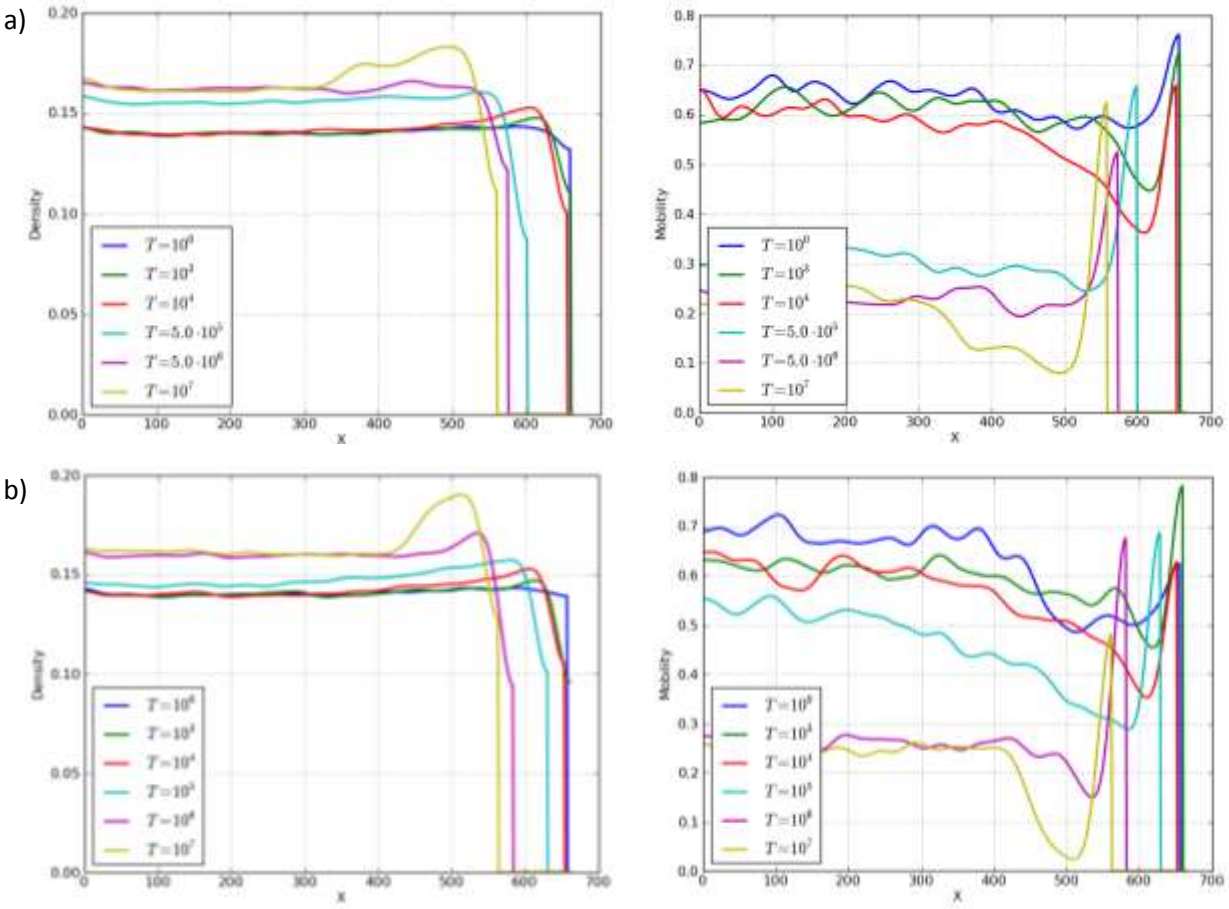


FIG 18 – System density and mobility as a function of the x-coordinate for different times ($N = 5 \cdot 10^4$). a) Low pressure, $P = 0.74$, b) High pressure, $P = 0.77$.

In the low pressure case, at times of order five times the relaxation time, one obtains a dense configuration, uniform along the sample, which remains metastable for at least another order of magnitude in time. This attests for an efficient transfer of the piston pressure to the whole system, on time scales significantly shorter than the nucleation times. In contrast, the high pressure case, by the time the density profile becomes flat and the pressure is efficiently transferred to the distant part of the sample, an even denser regime emerges next to the mobile boundary. This is manifested by the density peak at the right edge of the sample, and more pronouncedly by the mobility deep. As time goes on, this denser (nucleated) regime becomes more pronounce. Thus, in the low pressure regime, system (FIG 18 (a)), one may justify the

notion of a super-cooled state, but at higher pressure the emergence of a solidified "wall" occurs together with systems' relaxation to the super cooled state.

In conclusion, we find that a metastable super-cooled state is achievable only for $P \lesssim 0.75$. A typical higher pressure simulation will experience heterogeneous nucleation and phase separation before the inner liquid is exposed to the piston pressure. Once this solid inelastic wall is formed, the pressure of the piston is not transferred inside, and thus the liquid beyond the "solid wall" will equilibrate to a relatively low density, far below Random Closest Packing density. The R-Matrix theory expects a second order phase transition to occur at a pressure of $P_T \sim 0.83$[34], far beyond the reach of our simulation. Instead, the elastic boundary causes rapid creation of heterogeneous cluster nuclei, separating the inner liquid from the mobile boundary. Even without surface tension the system seems to rapidly phase separate at quite low pressures, surfacing the possible existence of a kinetic spinodal[12] in the $N_3$ system very close to the equilibrium transition pressure. This depends on homogeneous nucleation, and will be explored later in more detail. We are unable thus far to establish a method of delaying the heterogeneous nucleation, denying any hope of verifying the existence of a second order metastable phase transition with this implementation. The remaining portion of our work will concentrate on characterizing the super-cooled state where it exists, and exploring the nucleation processes observed in the system.

# 3. The Super-cooled State

In this chapter we concentrate on the super-cooled state in the regime where it is obtainable by simulation. First we find how deep we can delve into the super-cooled regime by filtering out phase separated realizations. The Equation of State, compressibility, and dynamic correlation functions are then explored, in the intent of finding behavior typical of glass formers.

## 3.1. Equation of state and compressibility of the system

To clearly define a super-cooled state, we require it exists for at least one time decade before succumbing to phase separation. Quite large systems, interesting enough for our purposes, exceed $2 - 3 \cdot 10^3$ particles, and take at least $5 \cdot 10^4$ time steps to relax completely (see FIG 12). This implies that the super-cooled state must exist at least until $T = 0.5 - 1 \cdot 10^6$ to be clearly defined.

We previously claimed that the super-cooled phase cannot be well defined for pressures exceeding $P \sim 0.75$. However, looking at specific realizations we find that while a sizable fraction of them undergo phase separation at times comparable to their relaxation, others remain in the super-cooled state for much longer times. Fortunately, it is simple to filter out the former. For this purpose, we define the solid fraction of a configuration as the fraction of particles having 4 closest neighbors surrounding them. The filters implemented check whether the solid fraction at the end of the simulation is significantly different than in the beginning (after relaxation). This notion of solid fraction, or more accurately cluster, will be further elaborated on later. We measured the solid fraction at the beginning and ending of the simulation over many realizations. Next we defined a "tight" filter, for realization initially within one standard deviation of the average solid fraction, and terminally within 1.5 standard deviations. Comparably, a "loose" filter was defined with limits of 1.5 and 1.8 standard deviations, respectively. Utilizing these filters, we present equation of state measurements for systems containing $5 \cdot 10^3$ and $10^4$ particles.

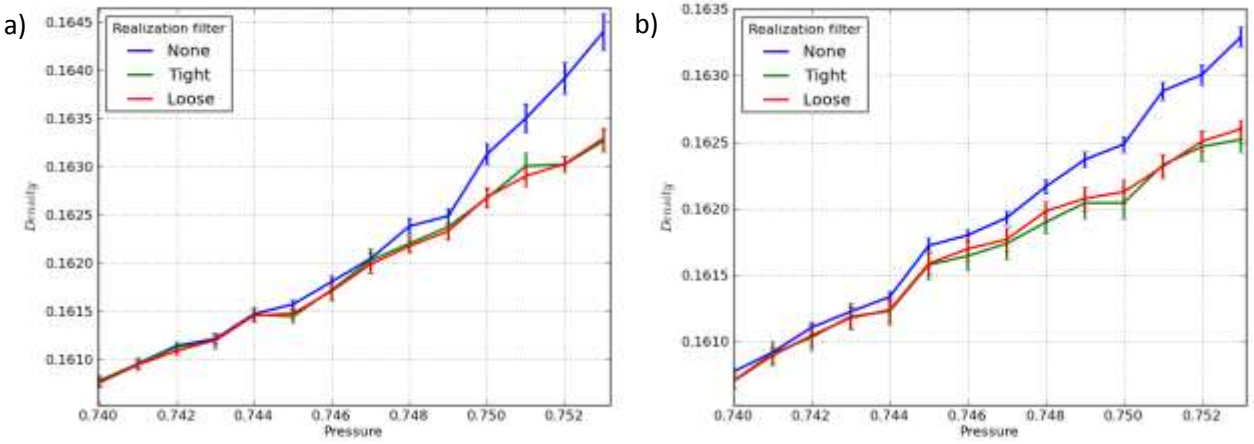


FIG 19 – Equation of state measurements with realization filtering. a) $N = 5 \cdot 10^3$, b) $N = 10^4$.

As suspected, higher pressures see the unfiltered equation of state start deviating from the filtered measurements. These are good news, as it potentially allows us to push the obtainable super-cooled phase deeper into higher pressures. However, the deviation of the unfiltered EoS implies that the fraction of realization failing the filtering procedure grows significantly. The next figure presents the percentage of realization passing the filters.

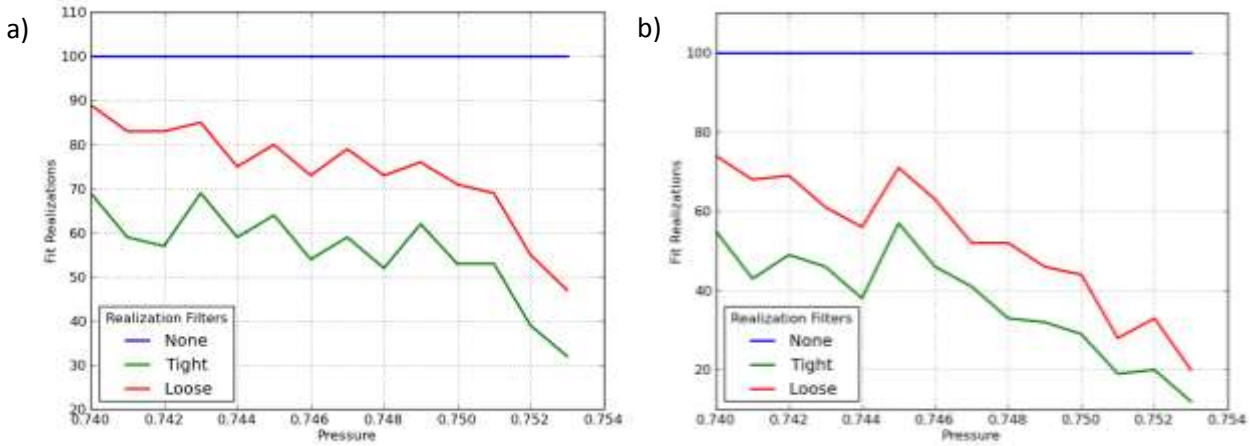


FIG 20 – Percentage of realization passing the filter as a function of pressure. a) $N = 5 \cdot 10^3$, b) $N = 10^4$.

FIG 20 demonstrates how the fraction of realizations passing the filters drops with higher pressure. The larger the system becomes, the faster the drop. This in turn corresponds to more realizations going through phase separation before a super-cooled state can be defined. For fairly large systems containing $10^4$ particles, only about 30% of the realizations exhibit a clear super-

cooled state for $P = 0.75$. Obtaining useful data on the super-cooled state becomes statistically challenging at higher pressures, but perhaps pressures up to $0.755$ can be reached with a reasonable efficiency of $5 - 10\%$. Larger systems fair even worse. We therefore have computational difficulties in producing meaningful results for pressures higher than $0.75$, which is, as mentioned earlier, far lower than the phase transition pressure expected by the R-Matrix theory ($P \sim 0.83$). In this chapter we shall thus limit our discussion about the super-cooled phase to the pressure range $P = 0.74 - 0.75$.

The (isothermal) compressibility $\chi_T = -\frac{1}{V}\frac{\partial V}{\partial P} = -\rho\frac{\partial \rho^{-1}}{\partial P}$ is an important measure of the system. As long as it remains capable of obtaining a super-cooled state, the system compressibility must smoothly increase, as the density increases smoothly with pressure. Any sort of phase transition should leave a clear mark on the compressibility, and thus it may lead to a useful way of detecting an incumbent transition. Although this observable can be inferred from the equation of state, we directly measure it by utilizing the fluctuation-dissipation theorem (FDT):

(26) $$\chi_T = \beta\frac{\langle V^2\rangle - \langle V\rangle^2}{\langle V\rangle} = N\beta\frac{\langle \rho^{-2}\rangle - \langle \rho^{-1}\rangle^2}{\langle \rho^{-1}\rangle}$$

Strictly speaking, we must take care when using this theorem, as it is invalid for glassy systems (or generally, systems out of equilibrium). It is thus important to let the system relax to local equilibrium before commencing with the volume averaging. As long as the initial condition of the system is of low density, and the pressure is not too high, starting the measurement after the relaxation times of FIG 12 ensures having an equilibrated system. The next figure shows the compressibility for filtered and non-filtered samples.

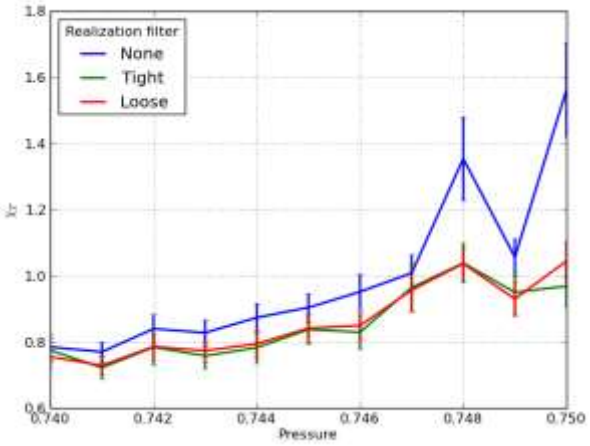


FIG 21 – Compressibility measurements for a $N = 5 \cdot 10^3$ system.

We find that the phase separation phenomenon, which becomes more prevalent in higher pressures, has a stronger footprint on the compressibility than on the density of the system. The non-filtered compressibility clearly deviates from the filtered measurement already at $P = 0.74$. Therefore utilizing the filters is crucial for obtaining the right compressibility values. In the explored pressure range the compressibility grows by about 25%, while the density increases only by 1%. This corresponds to significantly more density fluctuations in the deeper super-cooled regime. We observe a clear increase in the compressibility, but it is too far from the presumed singularity to confirm a second order phase transition.

## 3.2. Dynamic correlation functions

The defining mark of super-cooled states in glass forming systems approaching the glass phase transition is the two-step relaxation of a dynamic correlation function. Deep enough inside the super-cooled state, any dynamic correlation function should exhibit two distinct processes: $\beta$ (short time) and $\alpha$ (long time) relaxations. Separating the two relaxation processes is usually a well-defined plateau. The usual interpretation for those two steps utilizes the picture of local states existing in so-called geometric cages. The fast $\beta$-relaxation corresponds to configuration changes within a local cage, while the slow $\alpha$ relaxation describes the collective decorrelation of the individual cages on a macroscopic scale. The deeper the supercooling, the more stable the cages become, making the $\alpha$-relaxation process slower. In glass-like states the cages do not break, and the post $\beta$-relaxation plateau extends infinitely. Measuring a dynamic correlation

function will help us validate if the constant pressure $N_3$ system fits the glass former family in this aspect.

The most straightforward dynamic correlation function is the density-density correlation function, defined as the density average at two different times $t_1, t_2$[5]:

(27) $$C(t_1, t_2) = \frac{1}{N}\sum_{i=1}^{N}\langle\rho(t_1)\cdot\rho(t_2)\rangle$$

Since the system is in metastable equilibrium, the correlation function only depends on the time difference $t_2 - t_1$, and we may write:

(28) $$C(t) = \frac{1}{N}\sum_{i=1}^{N}\langle\rho(0)\cdot\rho(t)\rangle$$

In the $N_3$ lattice system the density of an occupied grid point is unity, and the density of a non-occupied point is zero. The function $C(t)$ thus counts the number of grid points occupied at both times, and divides the sum by the number of particles. The density-density correlation function may actually be defined in quite different ways, but this definition is adequate for our uses. The following figure depicts $C(t)$ measurements for systems of different pressures.

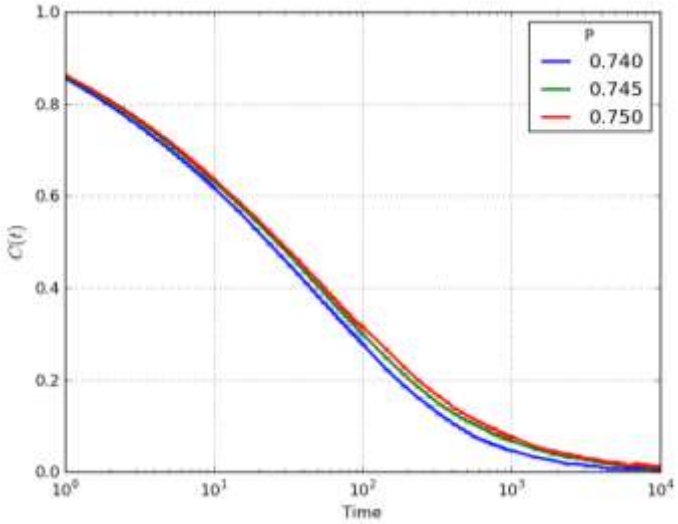


FIG 22 – Density-density correlation function for a $N = 10^4$ system. The 'Tight' filter was used to prevent phase separated samples from interfering with the measurement.

In FIG 22 there is no plateau and it seems that $\alpha$-relaxation starts at short times. The correlation decay resembles a stretched exponential of the form

(29) $$C(t) = exp\left[-\left(\frac{t}{\tau}\right)^{\gamma}\right]$$

with $\gamma \sim 0.35 - 0.4$. This form is typical for $\alpha$-relaxation, and is often related to heterogeneities in the sample. Suppose the system initially contains solidified clusters characterized by a broad spectrum of sizes. The larger a cluster, the longer we expect it remains correlated. Therefore a cluster size spectrum implies a broad decay of the dynamic correlation function. We shall later verify the existence of such a size spectrum, and its associated spectrum of relaxation times.

An important note must be presented on the analysis of unfiltered $N_3$ samples. We have seen that at higher pressure a larger fraction of realization do not stay super-cooled, but rather undergo phase separation through heterogeneous nucleation near the mobile boundary. Had one not noticed this behavior of the system, the results of dynamic correlation functions such as $C(t)$ would have been very different, and in fact actually resemble what would be expected of deeply super-cooled states in glass formers. High pressures are characterized by more frequent occurrence of large-scale clusters, which have very long correlation times. Clusters situated near the boundary are pressed directly by the piston, and may take even longer to decay. These clusters will result in the dynamic correlation function actually exhibiting a plateau typical of glass forming systems. The next figure illustrates such a case.

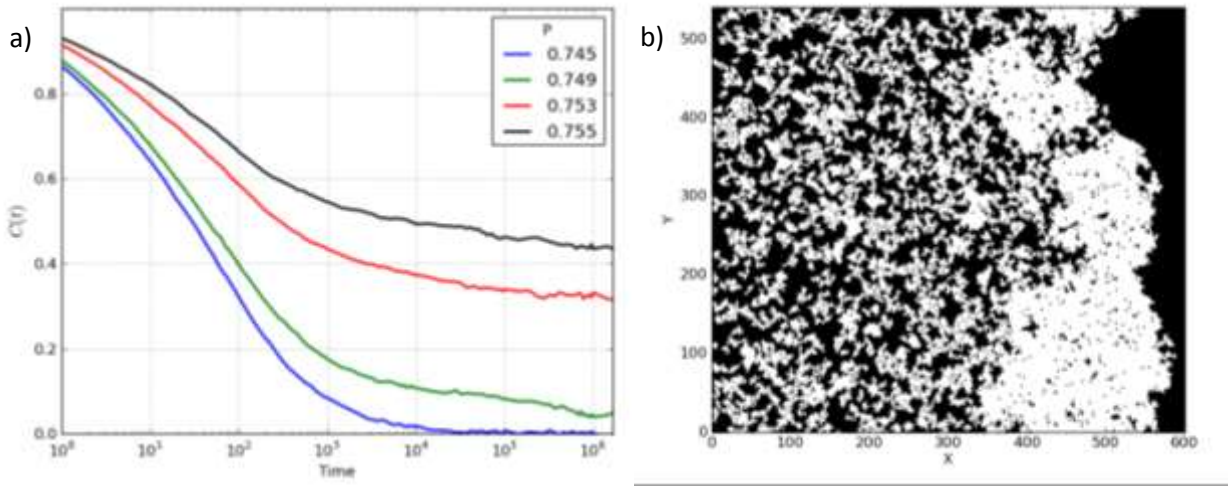


FIG 23 – Misleading results in non-filtered measurements of dynamic correlation functions. a) Density-density correlation function for different pressures. Higher pressures see the formation of a distinct plateau. b) An equilibrated ($P = 0.755, N = 5 \cdot 10^4$) sample showing large-scale clusters (in white) situated near the mobile boundary, causing the plateau formation in $C(t)$. The procedure used to mark clusters will be discussed in length in the following chapter.

The importance of filtering the samples is thus clearly demonstrated. Without filtering out phase separated samples dynamic correlation functions would exhibit misleading behaviors, typical of deeply super-cooled states or even glasses. As noted earlier, the phase separation occurring more rapidly in high pressure denies the effort of obtaining deeply super-cooled samples and validating whether the $N_3$ constant pressure systems conforms to the usual glass forming system behavior.

# 4. Nucleation

As comprehensively discussed in the preceding chapters, in a large fraction of samples the $N_3$ constant pressure simulator does not obtain the sought-after super-cooled states. Instead it ends up with rapidly forming phase separated configuration, consisting of liquid in rather low density, and solidified clusters. The largest of clusters seem to be formed through heterogeneous nucleation near the mobile boundary. However, homogeneous nucleation inside the sample apparently plays a significant role in the phase separation process, raising the option of a possible existence of a kinetic spinodal. In this chapter we will discuss the typical phase separation scenario found in the simulator runs, and mainly the creation of solidified clusters.

## 4.1. Cluster definition

The first step in analyzing the cluster formation processes observed in the system is to consistently and uniquely define a solidified cluster. Potentially many definitions can be used, and here we describe one quite simple definition. In the $N_3$ system particles do not occupy neighboring grid points. The closest particles may be placed at a distance of $\sqrt{5}$ unit lengths, in a way identical to a knight's move in chess. At most, a particle may have four nearby particles at the same distance. These particles can be ordered in two distinct ways, which we note as clockwise (CW) and counter-clockwise (CCW). The following figure clarifies this picture.

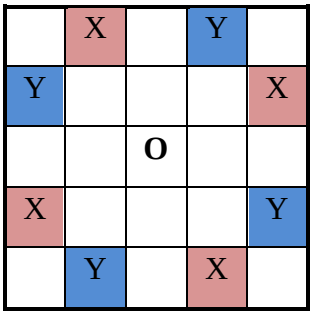


FIG 24 – Ordering options available for $N_3$ Clusters of the square grid. A central particle is positioned in "O". Neighboring particles may be positioned at a knight's move in either red "X" (CCW) or blue "Y" (CW) cells, but not in both cells separated by $\sqrt{2}$ and 2 unit lengths.

The entire system can be ordered ideally such that each particle is surrounded by four nearest neighbors in either CW or CCW formation. This will result in an optimal packing density of 0.2. For any configuration of the $N_3$ system, with particles located at $(x_i, y_i)$, We define a solidified

cluster as a set of contiguous particles residing on the same sub-lattice, having at least $m$ nearest neighbors positioned in either CW or CCW formation. All particles in the same sub-lattice should have their neighbors of the same type (CW or CCW). The parameter $m$ can take integer values in the range $1-4$. If a particle has one neighbor of one type and two neighbors of the other type, only the neighbors of the larger set are taken into account.

We now use the definition of clusters to analyze several types of configurations discussed above, e.g. the initial disordered state, the super-cooled state, the phase separated and the domain separated state. The following figure presents these system configurations, where we have highlighted the clusters on the liquid background.

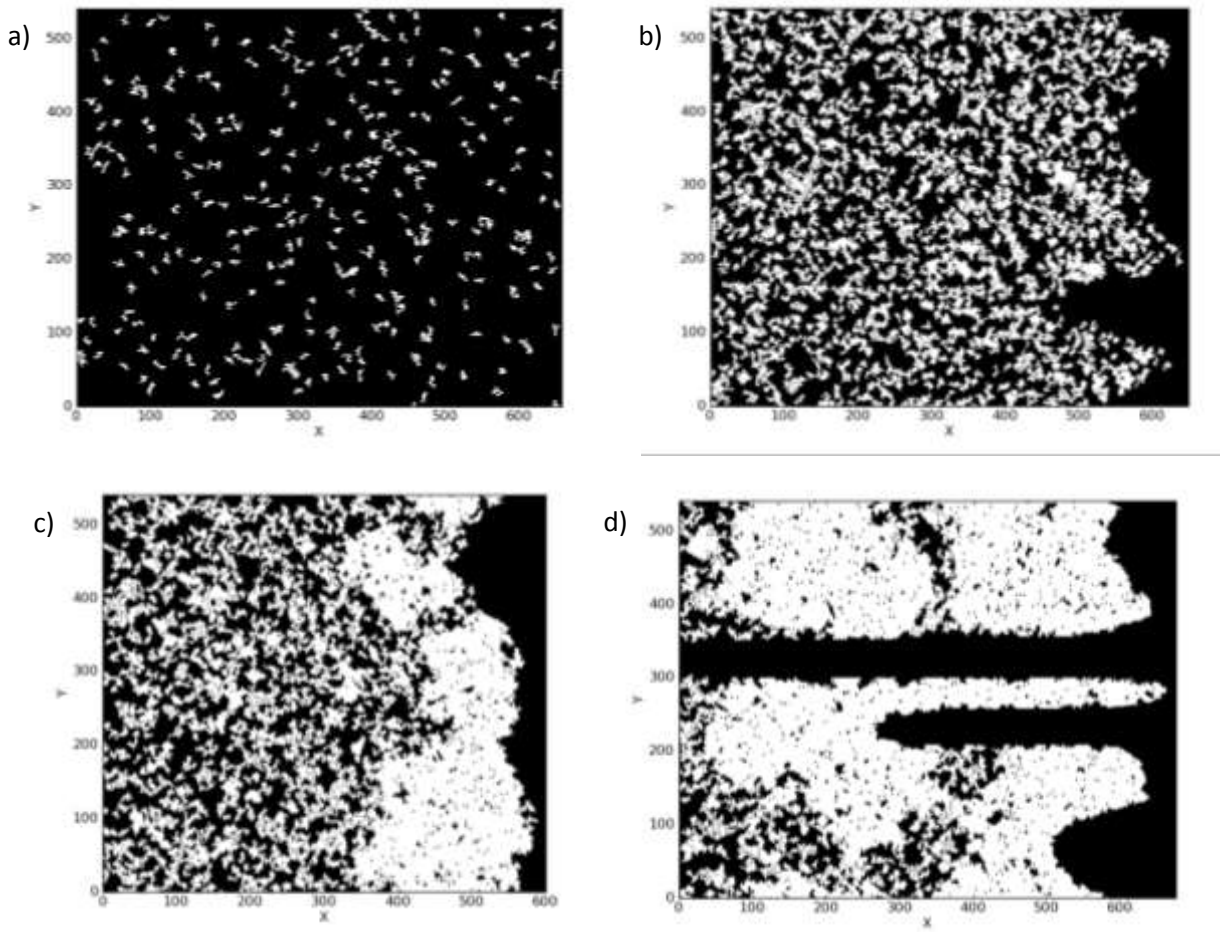


FIG 25 – Clusters in different $N_3$ states, simulated with $N = 5 \cdot 10^4$ and $\sigma = 0$. Clusters analyzed with parameter $m = 1$, are highlighted in white. Minimal cluster size was chosen to be 5 particles. a) Initial condition, almost devoid of clusters. b) "Equilibrium" super-cooled state ($P = 0.74$), characterized by many small clusters. c) Phase separated Equilibrium state ($P = 0.755$), with macroscopic clusters near the mobile boundary. d) Domain separated state ($P = 0.8$), identified by macroscopic void "fingers" penetrating deeply into the sample. Most of the particles are found in large solidified clusters.

We use here the choice $m = 1$. Choosing $m > 1$ does not change these pictures qualitatively. Setting positive surface tension in the range $0.05 - 0.1$ provides similar system states, with the formerly discussed benefits and disadvantages. FIG 26 presents states obtained by simulations augmented by surface tension with scale $\sigma = 0.05$. The particulate settings of these systems were depicted earlier in FIG 16.

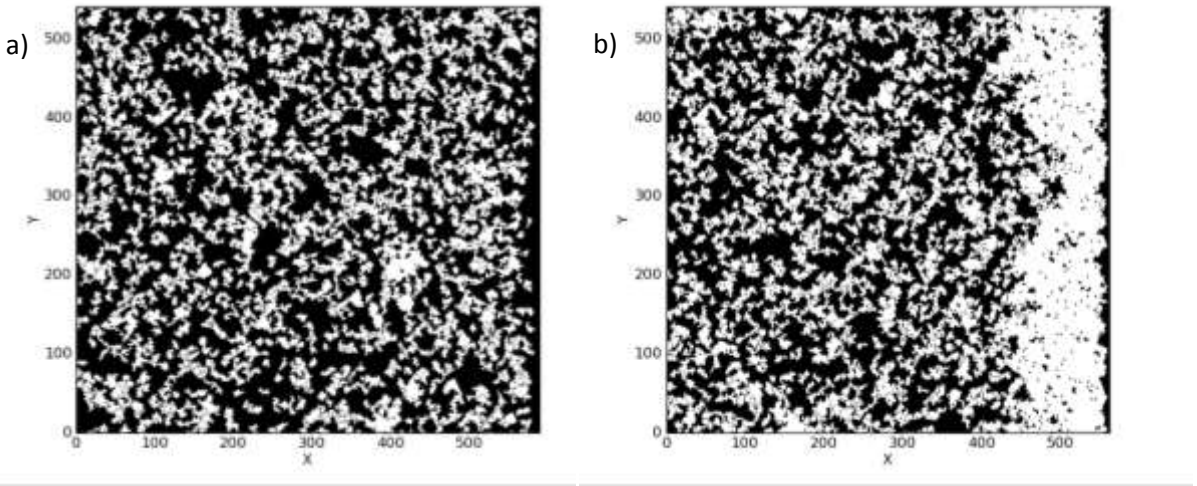


FIG 26 – Clusters in different $N_3$ states, simulated with $N = 5 \cdot 10^4$ and $\sigma = 0.05$. Neighbors parameter $m = 1$. a) "Equilibrium" super-cooled state ($P = 0.74$), b) Phase separated Equilibrium state ($P = 0.77$).

The clusters in the surface tension augmented systems are qualitatively similar to those observed with $\sigma = 0$. The surface tension straightens the mobile boundary, but phase separation is still clearly seen in pressures above $P \sim 0.75$. Due to the lack of domain separation in high pressures, these systems are easier to analyze. We thus explore cluster formation is systems with surface tension scale of $\sigma = 0.05$.

It is important to stress that the existence of clusters does not mean the system is solidified. Our simulations start with a random fluid-like initial condition, but even there many clusters can be found. The cluster number slowly increases as more clusters are nucleated. At long times larger clusters form partly due to merger of many small clusters. The total number of clusters should then decrease until a steady state is assumed by full equilibration or dynamical arrest of nearby clusters.

4.2. Properties of the clustering process

We first measure the number of clusters in the system as a function of time and pressure.

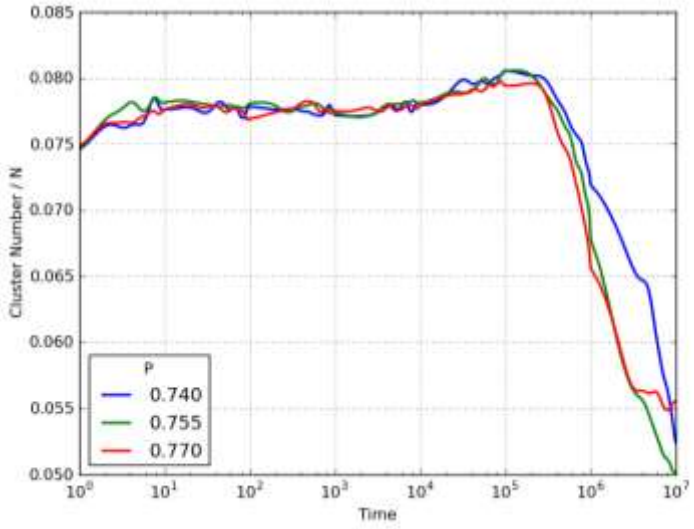


FIG 27 – Cluster number (divided by particle number) as a function of time for 3 different pressures ($N = 5 \cdot 10^4$).

FIG 27 generally conforms to the above scenario: The cluster number initially increases, and reaches a maximal value at $\sim 10^5$ time steps, which we term the *clustering timescale*. We have previously shown that this timescale marks the onset of the heterogeneous nucleation near the mobile boundary, or the phase separation. At this time clusters near the mobile boundary start growing, decreasing the total number of clusters in the system. Higher pressure runs seem to exhibit a faster decay of the cluster number. Interestingly, even for $P = 0.74$, where we have previously found the system to remain metastable up to $t \sim 10^7$, one observes that underlying processes of nuclei growth and merger do occur, even as the macroscopic density remains constant.

Next we check how the cluster sizes vary with time. We expect the average cluster size to sharply increase from the clustering timescale onwards. To demonstrate this, we plot the average, median, ant largest cluster size as a function of time.

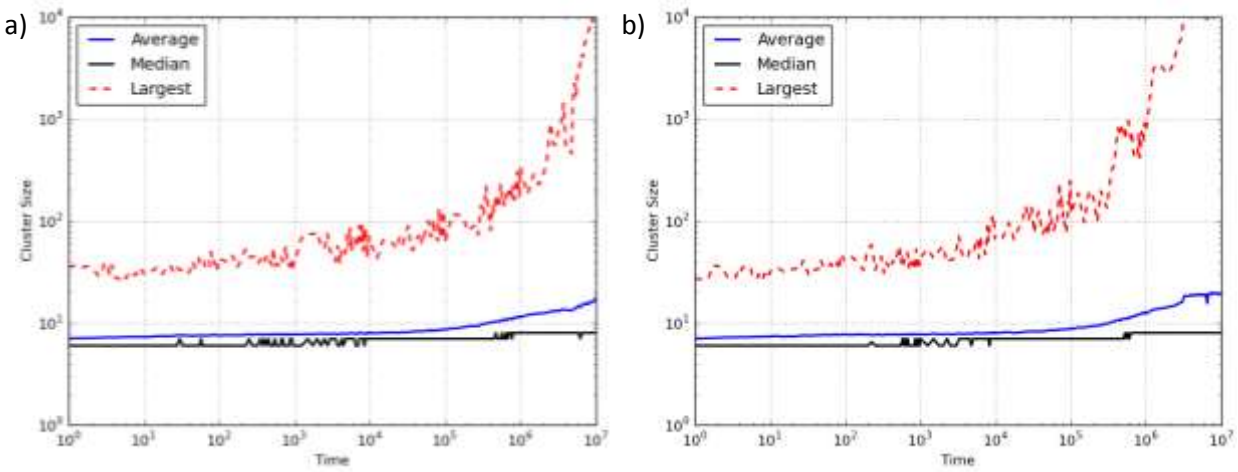


FIG 28 – Cluster average, median and largest size (number of particles) as a function of time measured for super-cooled and phase separated samples ($N = 5 \cdot 10^4$). a) Super-cooled ($P = 0.74$), b) Phase Separated ($P = 0.77$).

As expected, all systems demonstrate a rapid increase in the size of the largest cluster after the clustering timescale. Note that a giant largest cluster is formed even for low pressure, where no heterogeneous nucleation was observed, supporting the notion that homogeneous nucleation plays a role as well.

Using the improved understanding of the nucleation process, we may improve upon filtering crystallized realizations. The following figure demonstrates cluster average size measurements, and its standard deviation, for systems at different pressures.

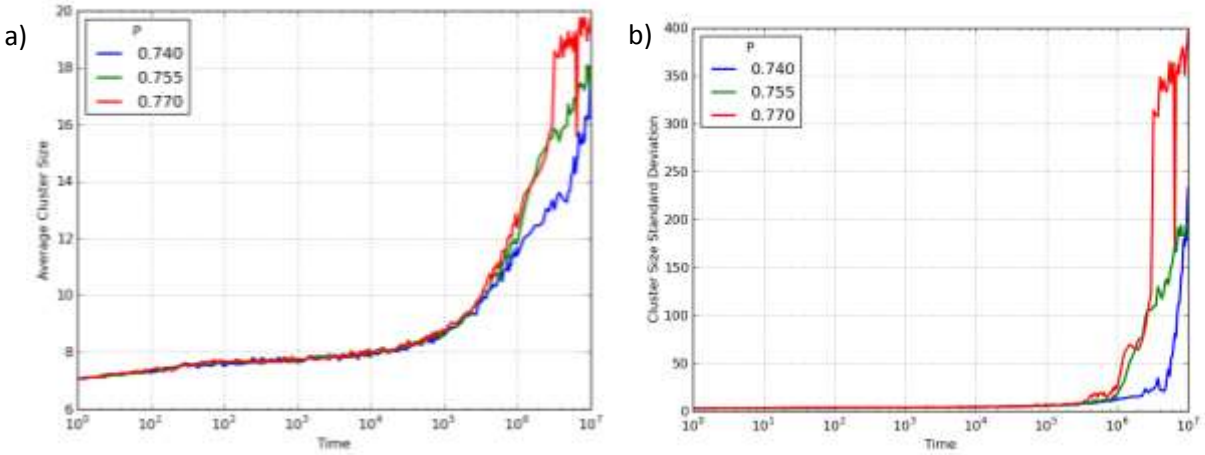


FIG 29 – Cluster average size and standard deviation as a function of time measured for three different pressures ($N = 5 \cdot 10^4$). a) Average cluster size, b) Cluster size standard deviation.

We note that a rapid growth of heterogeneous clusters near the mobile boundary is associated to a rapid increase in the size standard deviation. One may use this quantity to filter out nucleated systems, in order to better characterize the super-cooled, non-nucleated, configurations.

4.3. Classical nucleation theory and the $N_3$ model

Now that we have discussed the cluster formation in general terms, we shall try to place the findings in the framework of the classical nucleation theory (CNT)[1]. First suppose the system must be solid in true equilibrium. In the $N_3$ system, we know that to be true for pressures higher than about $P = 0.74$. Under these conditions the solid state is favorable with respect to the liquid. More accurately, a solid phase is characterized by lower Gibbs free energy than the liquid. This is true for each particle: at high pressures, every particle contained in a solid cluster lowers the total Gibbs free energy by some positive factor $\Delta G(P)$. CNT postulates that homogeneous nucleation occurs only when a critical sized cluster happens to form. Small clusters may easily be formed, but are just as easily dissolved. This can be thought of as a surface tension force which acts to dissolve small sized clusters. Surface tension is proportional to the surface of the cluster; it grows slower with cluster size, in comparison to the Gibbs free energy (which is proportional to the cluster volume, or size). The critical cluster size is thus derived from the competition between a surface and bulk term. In 2D, this notion can be formulated as follows:

(30) $S^* \Delta G = p^* \sigma_c$

Where $S^*$ is the critical cluster size, $\Delta G$ the Gibbs free energy gain per unit area of solid, $p^*$ the critical cluster perimeter, and $\sigma_c$ is the surface tension cost per unit perimeter length. The critical cluster size and perimeter are connected through a geometric link in the form

(31) $S = cp^{\varphi}$

Where $c$ is a constant, and $\varphi$ is usually expected to be $\frac{d}{d-1}$ ($d$ is the dimensionality of the system).

Realistically, it is impossible to calculate the values of $\Delta G(P)$ and $\sigma_c$ analytically in such a geometrically complicated system. To add complexity, these terms are not derived from energy variations between configurations (typically zero), but from entropic differences. Therefore, we

shall instead try to measure $S^*$ directly. Clusters smaller than $S^*$ should typically dissolve, while larger clusters should grow, given enough time. In other words, clusters larger than $S^*$ have a larger probability of accumulating particles, in comparison to the probability of losing particles. To measure the growth and decay probabilities we utilize the cluster cataloguing in each snapshot of the system. For each cluster in the catalogue, the possible moves that increase or decrease cluster size are counted separately. Next we define a growth ($P_{+i}$) and decay ($P_{-i}$) probabilities of cluster $i$ as

(32a) $$P_{+i} = \frac{M_{in,i}}{M_{in,i}+M_{out,i}}$$

(32b) $$P_{-i} = \frac{M_{out,i}}{M_{in,i}+M_{out,i}}$$

Where $M_{in,i}$ is the number of particle moves that increase the total size of the cluster, and $M_{out,i}$ is the number of particle moves that decrease the cluster size. The average net growth is then defined as the difference between the two probabilities:

(33) $$P_{Gi} = P_{+i} - P_{-i} = \frac{M_{in,i}-M_{out,i}}{M_{in,i}+M_{out,i}}$$

A negative $P_{Gi}$ means that cluster $i$ tends to dissolve, while positive $P_{Gi}$ means the cluster tends to grow. The higher the magnitude of the net growth, the stronger this tendency is. This measurement is in fact a crude first order estimate of the real net growth, as it does not account for series of moves, but only single particle moves from the snapshot measurement initial positions. The following figure presents net growth measurements as a function of cluster size, for a large system with $P = 0.74$ and $P = 0.77$.

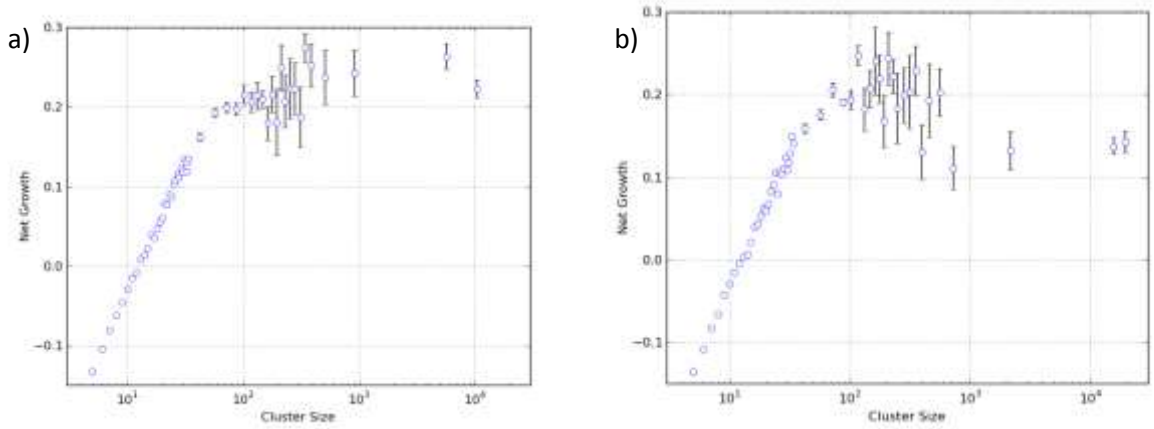


FIG 30 – Cluster net growth parameter as a function of cluster size ($N = 5 \cdot 10^4$). a) $P = 0.74$, b) $P = 0.77$.

These measured profiles generally confirm CNT expectations. Small clusters have negative net growth, indicating a tendency to dissolve. The larger the cluster, the more likely it is to grow. Cluster below the size of ~20-30 have excellent statistics, averaging to a clear $P_{Gi}(S)$ dependence. The critical cluster size, for which $P_{Gi} = 0$, is $S^* \sim 12$, and it is interestingly independent of pressure. The reason is that steady state liquid density has quite a slow dependence on the pressure beyond the phase transition. Larger cluster sizes have much worse statistics in comparison with the small ones, thus $P_{Gi}(S)$ spreads quite wide for $S \geqslant 30$. There is however a feature of this figure which is worth extra consideration. Very large clusters exceeding $2 \cdot 10^3$ particles always tend to grow, but clusters in the mid-range of $10^2 - 10^3$ particles show a very wide spectrum of probabilities. Some grow rapidly, but few actually tend to shrink due to a large perimeter. This range no longer fits the classical nucleation picture. These clusters are not nucleated but formed through nucleus growth. At some point many mid-sized clusters are formed. They start out isolated in a liquid surrounding, but eventually find other mid-sized clusters in proximity. Particle exchange between clusters, a complicated little understood process, then kicks in. This process is most likely responsible for the wide spectrum of probabilities observed in the $N_3$ system.

A word about the difference in $P_{Gi}(S)$ between super-cooled and phase separated states is in order. Qualitatively, the growth probability in phase separated states is quite similar to the super-cooled state. Both have the same critical cluster size $S^* \sim 12$ and the same behavior in the mid-range of the cluster size spectrum. The main difference between the two states occurs in the high range of the spectrum. Large clusters in a super-cooled sample tend to saturate at some net growth value, while in a phase separated sample, large clusters grow slower than mid-sized clusters. This phenomenon likely results from the role played by homogeneous nucleation. Phase separated samples form their clusters mainly through rapid heterogeneous nucleation and growth. These large boundary clusters reach their final size much more readily than slow growing homogeneously nucleated clusters. Moreover, boundary clusters may only absorb particles from one side, inevitably leading to slower growth.

As we have measured the critical cluster size, it is now possible to define the fraction of the system existing in solid state as the fraction of particles belonging to clusters larger than $S^*$. The

following figure shows the solid fraction of the sample as time progresses, and typical cluster size integrated spectrums.

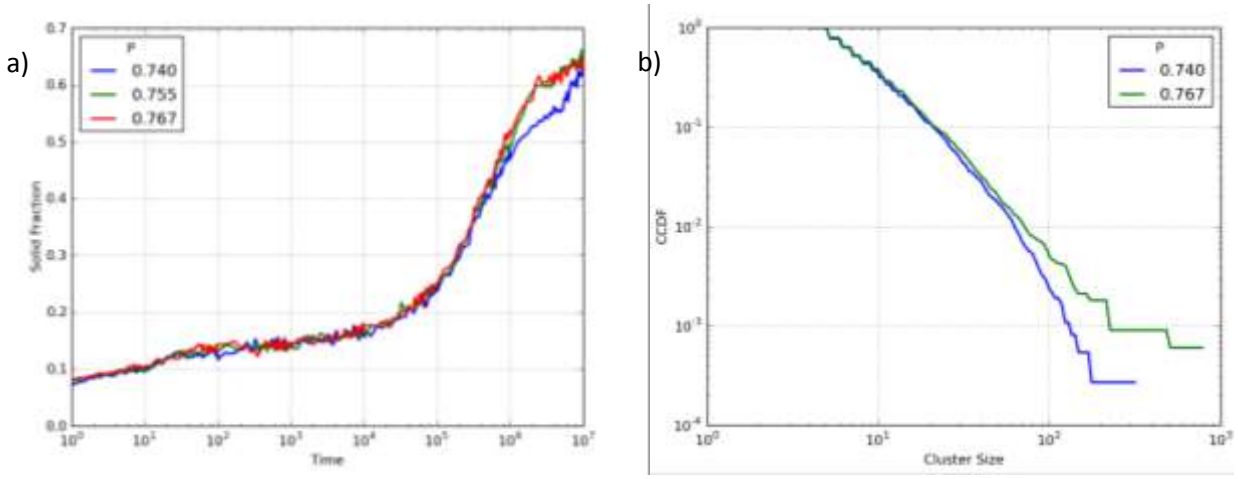


FIG 31 – Solid fraction as a function of time and cluster size integrated spectra. a) Solid fraction as a function of time for 3 pressures ($N = 5 \cdot 10^4$), b) Cluster size integrated spectrum (CCDF) for super-cooled and phase separated states ($t \sim 10^6$).

Perhaps quite disappointingly, there is no qualitative difference in the solid fraction measurements at different pressures following the clustering timescale ($t \sim 10^5$). Both super-cooled and phase separated sample exhibit a rapid rise in solid fraction, but a difference is observed following the solidified "wall" formation at $t \sim 10^6$. The super-cooled sample, devoid of solidified heterogeneous clusters has a somewhat lower rate of solid accumulation. This feature can be tied to the slower growth rate of homogeneous clusters. An important observation is that even the low pressure samples we considered super-cooled have a large fraction of supercritical clusters. This observation raises doubts as to our ability to achieve a metastable super-cooled state even at the lower pressure values studied. It is however only part of the story; supercritical clusters are not too much of a problem as long as they grow slow enough. Examining the CCDF of the cluster size, it is apparent that the clusters at low pressure are indeed smaller on average than in the higher pressure. Therefore, it is more likely that significant bodies of liquid remain intact between supercritical clusters for longer times.

The last facet of cluster formation we explore is the fractal dimension of the clusters. The fractal dimension may be defined by the power law that relates the cluster size and perimeter. The cluster perimeter here is defined as the number of particles which are part of the cluster but have

unoccupied neighboring spaces. In regular 2D shapes $S \sim p^2$, but the $N_3$ system clusters seem to behave rather differently. The following figure presents on a single graph the cluster size and its perimeter.

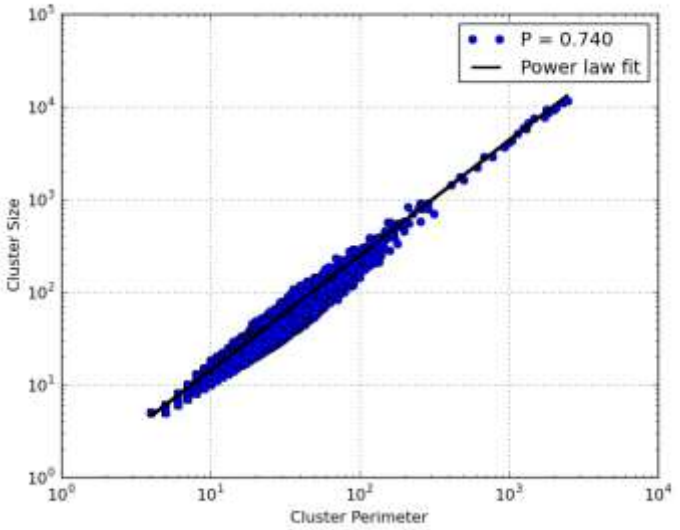


FIG 32 – Cluster size as a function of its perimeter ($P = 0.74,\ N = 5 \cdot 10^4$). A power law fit of the functional form $f(p) = 0.82 \cdot p^{1.24}$ is drawn in black.

As clearly shown in FIG 32, the cluster size obeys a power law in respect to the cluster perimeter. The power exponent is however very different from 2. The clusters in the $N_3$ system are therefore significantly ramified in nature. A survey of clusters indeed shows clusters having many extensions, protrusion and holes, which serve to rapidly increase their perimeter as cluster size increases. A fractal nature of the critical nucleation grains has implications for nucleation time estimates, and might serve as a hint for possible modifications of the CNT.

# 5. Conclusions

In this study we implemented a constant pressure Monte Carlo simulation of the $N_3$ model on a square lattice. This discrete extended exclusion zone model was thought to be a good case study for exploration of deeply super-cooled state of a simple amorphous material. We implemented the model using two distinct approaches, one following Pendzig et al.[20] (partial grid point), the other due to Nies and Cifra[42] (elastic boundary). Both approaches reproduce the known $N_3$ properties at low pressures and densities corresponding to the equilibrium fluid phase, but the partial grid point approach has proved to be very problematic at high pressures, particularly in large systems. The partial grid point was analytically analyzed and found to be inadequate in the thermodynamic limit due to an unavoidable growing energy gap. A proper modification to the choice of energy cost of particle occupation may fix this problem, but other energetic limitations, particularly at the low-$k$ region, may still render this approach unusable for large systems.

The elastic boundary approach fares somewhat better: by ensuring an intensive minimum volume variation we arrive at a robust implementation able to correctly simulate very large systems. An appropriate surface tension energy scale is nevertheless required, as systems devoid of any surface tension tend to form wildly curved boundaries and even separated non-interacting domains. The model was accompanied by a development of an efficient rejection free particle movement algorithm, supporting the simulation of large densely packed systems.

Local variable measurements show heterogeneities in the form of density/mobility gradients in the direction of the mobile boundary, hinting about a finite timescale for the outside pressure to seep deep into the sample. This creates further uncertainty about the actual pressure found in different locations. Methods to equate pressures everywhere in the system, or even an evaluation method of local pressure, were not implemented in this study. Their inclusion could potentially lead to significantly better results. Furthermore, other ways to control boundary curvature could be employed instead of the surface tension term. For example, one could implement a shear force, parallel to the mobile boundary, acting on the outermost particles. Such methods are expected to contribute to the production of more stable super-cooled samples, and thus may aid future exploration of the $N_3$ model in high pressures.

Once the implemented model was validated, we turned to explore the system properties in the little understood regime beyond the first order phase transition. There we found the expected super-cooled phase, which unfortunately does not seem to be stable far into the deeply super-cooled pressures. More specifically, at higher pressure heterogeneous cluster nucleation near the mobile boundary becomes more rapid and denies a clear distinction of a super-cooled state. Instead, a phase separated state is formed where the outer part of the system clusters up while the inner part remains mostly a low density liquid. We have shown that heterogeneous cluster nucleation is faster and more efficient than homogeneous nucleation, resulting in a "solidified wall" separating the inner liquid from the outside piston. Due to the hard-core nature of the particles, such a wall completely isolates the inner part from the piston, leaving it in a much lower pressure that the one applied externally.

Where heterogeneous cluster formation is rather slow, mainly in the pressure range $0.74 - 0.75$, homogeneous clustering is the lead cause of phase separation. Supercritical clusters with tendency to grow are rather abundant even in samples exhibiting smooth super-cooled properties. However, homogeneously formed clusters grow slowly, as their growth is impeded by mismatching surfaces of nearby clusters. Nevertheless, the observation of significant homogeneous nucleation suggests the possible existence of a kinetic spinodal. If that is indeed the case, any effort to avoid heterogeneous nucleation is futile and high pressure super-cooled states cannot be obtained. We cannot provide conclusive evidence on this matter, as it would require a method of pushing the super-cooled regime to higher pressures.

The most deeply super-cooled samples in our investigations were at far lower pressures than the theoretic R-Matrix predicted termination of the super-cooled phase. In pressures where a super-cooled state can be defined, no direct footprint of an incumbent glass transition was found in dynamic correlation functions. We observed an $\alpha$-relaxation phase which exhibits stretched exponential time dependence, suggesting spatial variation in the relaxation processes. This fact can be explained by the existence of a spectrum of clusters in varying size. Any such measurements must be conducted after filtering out phase separated samples, as their inclusion results in misleading behaviors of the dynamic correlation functions. In summary, the constant pressure $N_3$ square lattice model did not live up to the hopes of producing large high pressure

super-cooled state configurations. Despite our efforts, we are unfortunately unable to report new evidence of an incumbent ideal glass transition in this model. Possible ways to improve on the simulation method may lead to better results in the future.

## References

[1] Rate of Nucleation in Condensed Systems, D. Turnbull and J. C. Fisher, J. Chem. Phys. 17, 1 (1949).

[2] Under what conditions can a glass be formed? D. Turnbull, Contemp. Phys. 10, 5 (1969).

[3] The glass transition: Relaxation dynamics in liquids and disordered materials, E. Donth, Springer (2001).

[4] Dynamics of glassy systems, L.F. Cugliandolo, Les Houches 77, (2003).

[5] Super-cooled liquids for pedestrians, A. Cavagna, Phys. Rep. 476, (2009).

[6] Super-cooled liquids and the glass transition, P.G. Debenedetti and F.H. Stillinger, Nature 410, (2001),

[7] The Nature of the Glassy State and the Behavior of Liquids at Low Temperatures, W. Kauzmann, Chem. Rev. 43, 2 (1948).

[8] Kauzmann's paradox and the glass transition, R. J. Speedy, Biophys. Chem. 105 (2003).

[9] A tentative replica study of the glass transition, M. Mezard, G. Parisi, J. Phys. A: Math. Gen. 29 (1996).

[10] Glass transition and effective potential in the hypernetted chain approximation, M. Cardenas et al., J. Phys. A: Math. Gen. 31 (1998).

[11] Thermodynamical Liquid-Glass Transition in a Lennard-Jones Binary Mixture, B. Coluzzi et al., Phys. Rev. Lett. 84, 2 (2000).

[12] Glass and polycrystal states in a lattice spin model, A. Cavagna et al., J. Chem. Phys. 118, (2003).

[13] Viscoelasticity and Metastability Limit in Super-cooled Liquids, A. Cavagna et al., Phys. Rev. Lett. 95, 11 (2005).

[14] Computer simulations of super-cooled liquids and glasses, W. Kob, J. Phys.: Condens. Matter 11 (1999).

[15] Jamming: A new kind of phase transition? G. Biroli, Nature Physics 3, (2007).

[16] Replica approach to glass transition and jammed states of hard spheres, Giorgio Parisi and Francesco Zamponi, arXiv:0802.2180v1[cond-mat.dis-nn], (2008).

[17] Toward a mean field theory for spin glasses, G. Parisi, Phys. Lett. A 73, 3 (1979).

[18] The Classical Lattice-Gas Method, Yepez, J., ADA455835, 1999.

[19] Essays on Cellular Automata, A.W. Burks, University of Illinois Press, 1970.

[20] Constant pressure simulations of lattice gas models, P. Pendzig et al., J. Chem. Phys. 106, 9 (1997).
[21] Phase transition in three-dimensional lattice gas of hard-core molecules, J. Orban, Chem. Phys. Lett 3, 9 (1969).
[22] Triangular lattice gas with first- and second-neighbor exclusions: Continuous transition in the four-state Potts universality class, N. C. Bartelt and T. L. Einstein, Phys. Rev. B 30, 5339–5341 (1984) .
[23] Density functional theory for nearest-neighbor exclusion lattice gases in two and three dimensions, L. Lafuente and J.A. Cuesta, Phys. Rev. E 68, 066120 (2003).
[24] Monte Carlo simulations of two-dimensional hard core lattice gases, H.C.M. Fernandez et al., J. Chem. Phys. 126, 114508 (2007).
[25] Jamming, relaxation, and crystallization of a super-cooled fluid in a three-dimensional lattice, H. Levit, Z. Rotman, and E. Eisenberg, Phys. Rev. E 85, 011502 (2012).
[26] Phase transition in the hard square lattice gas, A. Bellemans and R.K. Nigam, Phys. Rev. Lett. 16, 23 (1966).
[27] Phase transition in a lattice gas with extended hard core, A. Bellemans and J. Orban, Phys. Rev. Lett. 17, 17 (1966).
[28] Phase transition in a lattice gas with third nearest neighbour exclusion on a square lattice, O. J. Heilmann and E. Praestgaard, J. Phys. A 7, 1913 (1974).
[29] First-order phase transition in hard-core lattice gases: I. Methods involving transfer matrices, R.M. Nisbet and I.E. Farquhar, Physica 76, pp. 259-282 (1974).
[30] First-order phase transition in hard-core lattice gases: II. Models on the square and triangular lattices, R.M. Nisbet and I.E. Farquhar, Physica 76, pp. 283-294 (1974).
[31] Phase transition in a lattice gas with extended hard core, J. Orban and D. Van Belle, J. Phys. A 15, L501 (1982).
[32] Random closest packing in a 2D lattice model, E. Eisenberg and A. Baram, J. Phys. A, Math. Gen. 33 (2000).
[33] A first-order phase transition and a super-cooled fluid in a two-dimensional lattice gas model, E. Eisenberg and A. Baram, Europhys. Lett., 71 (6), pp. 900–905 (2005).
[34] Ideal glass transition in a simple two-dimensional lattice model, Z. Rotman and E. Eisenberg, Phys. Rev. E 80, 060104(R) (2009).

[35] Direct Measurements of the Dynamical Correlation Length Indicate its Divergence at an Athermal Glass Transition, Z. Rotman and E. Eisenberg, Phys. Rev. Lett. 105, 225503 (2010).
[36] Glassy states in lattice models with many coexisting crystalline phases, M. J. de Oliveira et al., Europhys. Lett., 65 (1), pp. 20–26 (2004).
[37] Physics of simple liquids, W. W. Wood, edited by H. N. V. Temperly et al., North Holland Publications, Chapter 5 (1968).
[38] Computer simulation of liquids, M.O. Allen and D.J. Tildesley, Oxford University Press, Chapter 4 (1989).
[39] NpT-ensemble Monte Carlo calculations for binary liquid mixtures, I.R. McDonald, Molecular Physics 23, 1 (1972).
[40] Monte Carlo simulations of phase equilibria for a lattice homopolymer model, A.D. Mackie et al., Europhys. Lett. 27, 549 (1994).
[41] Monte Carlo simulations of phase equilibria for a lattice homopolymer model, A.D. Mackie et al., J. Chem. Phys. 102, 2 (1995).
[42] Equation of state behaviour and interfacial properties of lattice chain fluids: A comparison of lattice fluid theory and Monte Carlo simulation, E. Nies and P. Cifra, Macromolecules 27, (1994).
[43] Equation of state calculations by fast computing machines, N. Metropolis et al., J. Chem. Phys. 21, 1087 (1953).

# Appendix: Technical aspects

I. Basic numerical implementation

The first step in the exploration and computation of the $N_3$ system is implementing the system in a simple and efficient numerical scheme. Implementing the $N_3$ system in isothermal-isobaric conditions requires some refined consideration. First, we wish our scheme may be able to handle systems with as many particles as possible, as to approach the thermodynamic limit. This requirement imposes the heaviest restrictions on our scheme. Larger systems require more computation to achieve the same computed time scales, and more memory to handle the system information. In large systems of the scale we wish to explore, efficiency turns out to be a more restrictive than information capacity. Another hurdle we have to overcome is allowing the system to expand and contract, as its volume may change at every new sampled configuration. In chapter 1 we have discussed how to define a mobile system boundary such that sampled configurations expanding the system would be permissible in reasonable time. Now we need to use this knowledge to implement a mobile boundary.

The basic structures required for implementation of the 2D $N_3$ model are two data arrays. The first array represents the grid (shall be called *GRID*). This is a 2D array representation of the particle locations on the lattice, and it is defined as described in the following:

1. The first dimension in *GRID* represents the x-axis, and the second dimension represents the y-axis.
2. If location $(x, y)$ is occupied by a particle tagged as an integer $i$, the matching $(x, y)$ cell in *GRID* is set to the particle tag $i$. As discussed, the particle may be viewed as 5-celled crosses. When we speak of an occupied location we always mean the center grid point of the cross shaped particle.
3. If location $(x, y)$ is in the exclusion zone of $j$ different particles, the matching $(x, y)$ cell in *GRID* is set to the value $-j$. Note that this marking is very useful to determine which particle moves are allowed. A particle move may be accepted if and only if the *GRID* value in its new considered location is $-1$ (i.e. it is only in the exclusion zone of itself).
4. If location $(x, y)$ is not in the exclusion zone of any particle, the matching $(x, y)$ cell in *GRID* is set to the value $0$.

A figurative example for the structure *GRID* is hereby described. Suppose our system is of size 6x6 and composed of 4 particles in positions (1,6), (2,4), (4,2), (5,4), marked as 1, 2, 3 and 4 respectively. The resulting array *GRID* is shown in FIG A1. We remind that our system has cyclic boundary condition on the y-axis, and closed boundary condition on the x-axis.

| | | | | | | |
|---|---|---|---|---|---|---|
| 6 | **1** | -2 | -1 | -1 | -1 | 0 |
| 5 | -2 | -2 | -1 | -1 | -1 | -1 |
| 4 | -2 | **2** | -2 | -3 | **3** | -1 |
| 3 | -1 | -1 | -2 | -2 | -2 | -1 |
| 2 | -1 | -2 | -1 | **4** | -2 | -1 |
| $y = 1$ | -1 | -1 | -1 | -1 | -1 | 0 |
| $x =$ | 1 | 2 | 3 | 4 | 5 | 6 |

FIG A1 – An example of the *GRID* array for a simple 6x6 system with 4 particles. Particle locations are stressed in bold and grey background.

In a system where the volume may change during the simulation, it is required to make the size of the *GRID* array variable, or at least make it large enough to contain all reasonable volume variations. Since our system may change volume only via the right x-axis boundary, its length on the y-axis is always a constant $D$.

The second basic data structure is a representation of the system from the particle point of view. We have seen in *GRID* that each particle is tagged by an integer. We can use this integer tag as an index of a new 2D array of size $Nx2$ ($N$ – the total particle number). This structure will henceforth be named *LIST*. For now it contains the location of each particle on the grid, but in a following refinement of the numerical scheme this data structure will be augmented. *LIST* is defined such that its (i,1) cell contains the $x$ location of the i$^{th}$ particle, and the (i,2) cell contains the $y$ location of the i$^{th}$ particle.

Clearly the two data structures described above contain the same information, and each one could easily be built from the other. However, both have advantages and disadvantages which justify keeping both of them updated at all times. The *GRID* structure is a straightforward representation of the system, and eases the effort of checking whether a particle move is allowed

or not. On the other hand, *LIST* provides a concise description of all particle information, and quick access to a particular particle by its tag.

Another system detail that must be accounted for is the representation of the mobile boundary location. When the boundary is a straight line (as in the partial grid point method), it is sufficient to note its $x$ location only. However, when the mobile boundary curves and has a local $x$ position, we indicate this by a 1D array $L(y)$.

II. Initial conditions

We now have all the data structures we need to establish a simple Monte-Carlo simulation scheme for the $N_3$ system in isothermal-isobaric conditions, but we still require an initial condition. This can be achieved in various ways. The simplest of them is setting the system size and randomly placing particles until the required number $N$ is met. This is however not a useful technique since it arrives at very low initial densities. We wish to explore the high density region of the Equation of State (EoS), near and beyond the phase transition, so we would like to have an initial condition with a rather high density. A method to achieve this goal is rather straightforward. We initially set a rather small system size (e.g. such that results in very high optimal packing density), and randomly place particles in it. If there is no room left to place more particles, we expand the system somewhat by furthering the mobile boundary. This algorithm recurs as long as needed to place all the $N$ particles. The aforementioned initial condition method typically achieves densities in the vicinity of $0.14$ (close to the density achieved by Random Sequential Adsorption procedures[32]), a reasonable initial condition for our uses.

There are two other methods we employ to obtain a suitable initial condition. Both of them simulate particle movements to obtain high packing densities. The first method can be viewed as system quenching: We press the system (with a straight mobile boundary) in infinite pressure for a given time, arriving at densities close but lower than the random closest packing (RCP) density. A different technique is called random sequential adsorption diffusion (RSAD). We initially set the system size as to conform to a predefined system density $\rho$. Then we randomly place particles until the initial volume fills. When there is no more room to place more particles,

we let the particle diffuse, waiting for a permissible location to form. Every time a room for a new particle clears, it is immediately filled, until the final particle number $N$ is met. These methods are used when we wish to start the simulation in very high densities (in excess of $0.16$), e.g. for sanity checks of the simulator.

III. Particle movement selection protocols

The simplest approach to simulating particle movements in the $N_3$ system will be henceforth referred to as "Random Selection" (RS). It may be thus described:

1. Randomly select a particle and movement direction. We shall call this a particle move. This protocol amounts to randomizing two integers, a particle tag in the interval $1,\ldots,N$, and a direction indicator in the range $1,\ldots,4$ (right, up, left, down respectively).
2. Check if this particle move is allowed by the rigid-body potential of its neighbors (As aforementioned, the *GRID* value in the new particle position must be $-1$). If so, calculate the energetic cost of this movement.
3. Try the particle move with the Metropolis criterion. If the move passes this criterion, perform it.
4. Change the position of the mobile boundary if needed.
5. Update the relevant data structures.

Using the RS approach, it was quickly discovered that the method is insufficient to simulate high density systems. In step 2 of the algorithm we check if a certain random move is allowed by the moving particle's neighbors. The move validity check is usually passed in low density states, when particles are far away from each other. In high density systems however, particles are located in high proximity and most random moves are forbidden. When randomly choosing a particle and move direction in a high density system, we usually try a move that has zero probability of acceptance, wasting computation time. Therefore, in high enough density, this protocol spends most of the time on attempting impossible particle moves, leading to low efficiency.

A more efficient method for dense systems is clearly in order. The scheme we implemented lets the system choose random particle moves, but only from an updated set of moves that are *known*

to be allowed by the rigid-body potential. We refer to the enhanced method as "Rejection Free" (RF). The new approach requires an extension of our system data structure; we define a new 2D array which stores the current rigid-body allowed particle moves, named *MOVES*. This array shall store all the allowed particle moves in some order, and must contain information on the particle which moves and the movement direction. Therefore, the array *MOVES* is of size $Mx2$, where $M$ is the number of currently allowed particle moves. Array *MOVES* is defined such that its (m,1) cell contains the tag of the particle $(1,..,N)$ moving by utilizing the $m^{th}$ move, and the (m,2) is the direction $(1,...,4)$ that this particle moves to. A complementary integer variable *nMOVES* holds the current total rigid-body allowed moves. To save computation time, we initially set the size of *MOVES* to $4Nx2$, the maximum number of allowed particle moves, avoiding repeated copying and reallocation of the array. To conclude the scheme we must connect the previous data structures to the new array. A practical way of doing it is augmenting the *LIST* array; its size grows from $Nx2$ to $Nx6$. The new data cells contain references from the particle tag to the particle's available moves. Cell (i,d+2) now contains the movement number that the particle utilizes in moving to direction $d$ $(1,...,4)$. For example, Cell (1,3) contains the move number in *MOVES* for the movement of the $1^{st}$ particles to its right direction. If a move is not allowed due to rigid-body potential, its respective cell is set to zero.

These definitions conclude the data structures used by our numerical scheme, but we must still overcome a significant hurdle to effectively implement the Rejection Free method. An efficient protocol for updating the data structures for each new configuration must be developed. In the RS method, the protocol of updating the arrays *GRID* and *LIST* in $O(1)$ is trivial. We simply "move" the particle one block in *GRID*, and set the *LIST* entry of its tag accordingly. The RF algorithm poses a more difficult problem. It is insufficient to update only the moving particles' information, since its very movement may affect the allowed movements of its neighbors. Checking a particular movement direction for a particular particle is easy enough. One just has to check if the *GRID* cell in that direction has the value $-1$. In order to achieve $O(1)$ efficiency, we need to apriori indicate which moves of which particles have to be checked for validity. The following figure shows an example of the points in *GRID* that have to be checked.

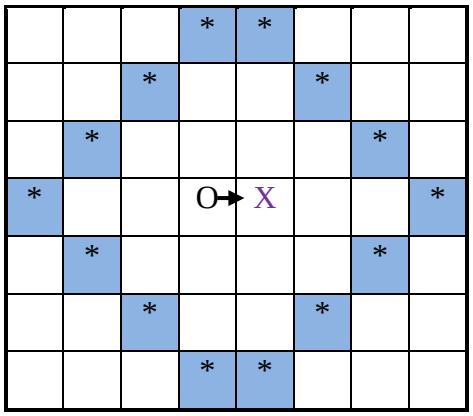


FIG A2 – GRID regions affected by particle movement. A particle in position "O" moves right to a new position "X". The cells containing asterisks (accentuated with blue background) indicate locations where particle allowed movements are affected by this move.

It can be shown that for every possible particle move, at most 14 adjacent particles are affected. Checking these 14 points around the moved particle results in an $O(1)$ updating protocol. Further refinement of this protocol is possible, since every one of those 14 supposed particle locations are affected differently by the movement. However, simply checking all move directions of all existent particles in these 14 locations provides a satisfactorily efficient updating protocol.

The refined approach to particle movement simulation, the Rejection free algorithm, can be thus summarized:

1. Randomly select a movement number. This is done by randomizing one integer, a move indicator $m$ in the interval $1,\ldots,nMOVES$. Extract from the chosen move which particle performs the movement, and to what direction.
2. Calculate the energetic cost of this movement. The energy variation will typically be zero, unless the particle move occurs near the mobile boundary, changing the volume.
3. Try the particle move with the Metropolis criterion. If the move passes this criterion, perform it.
4. Update the data structures *GRID* and *LIST* for the moved particle.
5. Update the permissible moves of the moved particle. These are accessible via the particle *i*'s data structure *LIST(i,d+2)*. Update the total number of moves *nMOVES*.
6. Check the 14 adjacent locations (visualized in FIG A2). If they contain particles, update their permissible moves. Update the total number of moves *nMOVES*.
7. Change the position of the mobile boundary if needed.

IV. Time evolution of the system

An important notion we must still make clear is the system time step. A system time step is defined as the time at which each particle attempts one movement to every permissible direction, in average. For example, in very low densities (ideal gas) containing $N$ particles, one time steps would be $4N$ particle movements ($N$ particles x 4 movement directions). Note that this does not mean that every particle must move 4 times to complete a time step, but only that there must be $4N$ movement attempts of *any* particle.

In the Random Selection approach, a time step thus means $4N$ configuration samples. The true benefit of the Rejection Free approach is that a time step in this algorithm is just *nMOVES* configuration samples, which may be significantly less than $4N$. This means that a RS time step takes a constant amount of real time to compute, regardless of the system density. A RF time step computation time is proportional to the total allowed number of moves, which decreases the higher the system density. We may now formalize the time advancement in terms of configurations sampled by the simulator: Each sampled configuration in the RS approach advances time by $\Delta t_{RS} = [4N]^{-1}$; each sampled configuration in the RF approach advances time by $\Delta t_{RF} = [nMOVES(t)]^{-1}$. It may be more accurate to sample $\Delta t_{RF}$ from an exponential distribution with average $\Delta t_{RF} = [nMOVES(t)]^{-1}$, but this choice negligibly affects the long range time evolution. Since in high density systems $nMOVES \ll 4N$, typically $\Delta t_{RF} \gg \Delta t_{RS}$.

V. Random Selection (RS) vs. Rejection Free (RF) algorithms

The advantage of the Rejection Free approach is clear. Using it, we waste no computation resources on moves which are apriori impossible due to the rigid-body potential. At least in dense configurations, such an approach may greatly increase the number of configurations sampled for a given amount of real time. However, in low enough densities, the Random Selection algorithm may be faster. It is interesting to check in which region of the density map one approach surpasses the other in computational efficiency. In the following figure we show the total number of moves vs. the system density. Next to it displayed the real time taken for a constant amount of particle movement tries vs. the system density.

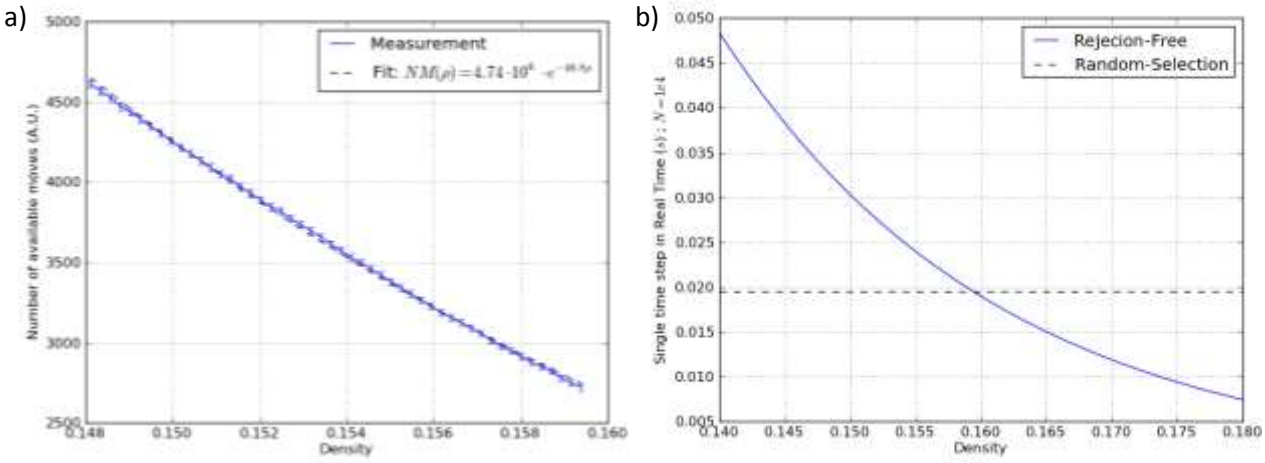


FIG A3 – Random Selection vs. Rejection Free algorithms. a) The number of allowed moves shows a sharp decrease when approaching the phase shift density of ~0.16. b) Rejection Free approach surpasses the Random Selection in terms of efficiency somewhat below the phase transition density, justifying its use in the super-cooled regime.

From FIG A3 it can be shown that at rather low densities, there are many permissible particle moves, making the Random Selection approach more efficient. In high density systems, the number of permissible moves drops sharply as the neighboring particles grow closer. This is mirrored in improvement of the Rejection Free approach, finally surpassing the Random Selection approach somewhat below the density 0.16. At higher still densities, the Rejection Free approach is clearly superior, gaining more efficiency as the total number of permissible moves decreases.

## VI. Data analysis

In this work we generally separate between the actual thermodynamic simulation and the data analysis required to obtain most meaningful results. For maximum computational efficiency, the simulator is implemented in Fortran90. On the other hand, the data analysis is performed in post processing using Python. To allow post processing by an outside script, we export the *LIST* data structure from the simulator at different times into a text output file. Alongside the *LIST* array we export measurement times and volumes (or densities). This output represents "snapshots" of the system at known times, enabling both static and dynamic observables to be calculated in a straightforward manner. The times at which system snapshots are taken is predefined in the simulator. We usually choose a constant amount of snapshots in each time decade (20-35), a

choice which establishes logarithmic resolution in time. The measurement starts at time zero, whose density can be set by the user with the initial condition. Instead, a predefined "equilibration time" may be used to delay measurement commencement. These setting can be used to allow the system to reach equilibrium before starting to take measurement snapshots.

In the chapter exploring cluster formation we have theoretically described a method of cataloguing clusters in a given system snapshot. The algorithm that was used to implement this method is described here. It starts with the first particle on the LIST data structure, and recursively jump to CW or CCW positions (defined in FIG 24). Verified neighboring particles are then located and added to the cluster list. CW and CCW formation are checked independently, and the larger is set to contain each particle. The recursion ends when all particles in the system are catalogued to clusters (or left as liquid). This algorithm ensures we end up with the same clusters no matter which particles are checked first.

## תקציר

כאשר מקררים חומר מתחת לנקודת ההתכה שלו, הוא עובר למצב הנקרא נוזל מקורר ביתר. בחלוף הזמן, יהפוך הנוזל המקורר ביתר לגביש מוצק יציב, או ייכנס למצב אמורפי הנקרא זכוכית. טבעו של מעבר הפאזה הזכוכיתי, החל עמוק במשטר הנוזלים המקוררים ביתר, עודו אחת השאלות הפתוחות בפיסיקה של חומר מעובה. מעבר זה לא ניתן לצפייה ישירה בניסוי או בסימולציה, מאחר שזמן הרלקסציה צפוי להתבדר בנקודת מעבר הפאזה.

כחלק מהניסיון ללמוד את מאפייני הנוזלים המקוררים ביתר, במיוחד עמוק במשטר זה, אנו מציעים לחקור מודל פשוט יחסית של נוזל סריגי, מודל ה-$N_3$ בעל האזור האסור המורחב. ידוע כי מערכת זו, בה אין אינטראקציות ארוכות טווח בין החלקיקים, נתקעת במצבים אמורפיים בצפיפויות גבוהות. על מנת לחקור את המודל, בחרנו במימוש של סימולציה שוות-לחץ. שיטה זו נבחרה משום ששיטות שוות-נפח הינן פחות יציבות עבור נוזלים מקוררים ביתר.

המימוש של סימולטור שווה-לחץ לנוזל סריגי כרוך בסיבוך מסוים, מאחר שאסור להפרשי הנפח בין שתי קונפיגורציות דגומות להיות גדולים מדי. מימשמו את המודל בלחץ קבוע באמצעות שתי שיטות שונות, הראשונה בעקבות .Pendzig et al, והשנייה לפי Nies & Cifra. השיטה הראשונה נמצאה כלא מתאימה למערכות גדולות, בעוד השנייה מצליחה יותר בתחום זה. דגימות נוזל מקורר ביתר הושגו בתחום לחצים שלא היה זמין בעבר. לעומת זאת, הדגימות המקוררות ביתר בלחצים הגבוהים ביותר שהושגו עדיין רחוקות מהנקודה הצפויה למעבר הפאזה לזכוכית האידיאלית.

הנוזל המקורר ביתר נחקר היכן שהדגימות זמינות. לא נמצאו סימנים להתקרבות לנקודת מעבר הפאזה הזכוכיתי במדדים כדוגמת פונקציות קורלציה דינאמיות. תהליך ההתגבשות (נוקלאציה וגדילת הגרעינים), שמגביל אותנו בקבלת נוזלים מקוררים ביתר בלחץ גבוה, נחקר גם הוא. נמצא כי תהליכים הומוגניים והטרוגניים הם בעלי תפקיד חשוב ביצירה של גושים מוצקים. גושים אלה הינם מסועפים מטבעם, תצפית שעשויה להוביל לסטיות מתאוריית הנוקלאציה הקלאסית.

אוניברסיטת תל-אביב
הפקולטה למדעים מדויקים
ע"ש ריימונד ובברלי סאקלר

# סימולציות שוות-לחץ של נוזל מקורר ביתר על סריג

חיבור זה הוגש כחלק מהדרישות לקבלת התואר

"מוסמך אוניברסיטה" – M.Sc. באוניברסיטת תל-אביב

בית הספר לפיסיקה ואסטרונומיה

המחלקה לחומר מעובה

על ידי

**מנחם (נחי) שטרן**

העבודה הוכנה בהדרכתו של

**פרופ' אלי אייזנברג**

דצמבר 2012